Hindawi
Structural Control and Health Monitoring
Volume 2024, Article ID 9995641, 22 pages
https://doi.org/10.1155/2024/9995641

Research Article

Gust Factor Approach for Estimating Maximum Response and Control Force in High-Rise Base-Isolated Buildings with Active Structural Control

Yinli Chen,[1] **Daiki Sato**,[2] **Kou Miyamoto**,[3] **Jinhua She**,[4] **and Osamu Takahashi**[1]

[1]*Department of Architecture and Building Engineering, Faculty of Engineering, Tokyo University of Science, Katsushika, Tokyo 125-8585, Japan*
[2]*Institute of Innovative Research, Tokyo Institute of Technology, Yokohama, Kanagawa 226-8503, Japan*
[3]*Institute of Technology, Shimizu Corporation, Koto, Tokyo 135-8530, Japan*
[4]*School of Engineering, Tokyo University of Technology, Hachioji, Tokyo 192-0982, Japan*

Correspondence should be addressed to Yinli Chen; yinli.chen@rs.tus.ac.jp

Received 9 August 2023; Revised 3 February 2024; Accepted 1 March 2024; Published 22 March 2024

Academic Editor: Lin Chen

This paper devises a new method for estimating the maximum response and maximum control force for high-rise base-isolated buildings with active structural control (active base isolation) to simplify the conventional complex design procedure. While active base isolation has emerged as a prominent solution for achieving high control performance, its design process is inherently complex, particularly when applied to high-rise buildings where wind loads become prominent. To address this problem, we propose a streamlined method inspired by the gust factor methodology widely used in conventional passive wind-resistant designs. This method estimates the maximum response and maximum control force without the need for numerical simulations. We first construct an equivalent passive model of a multi-degree-of-freedom control system to theoretically compute the dynamics of the system. Based on the constructed equivalent passive model and then propose a method to calculate the mean displacement and mean control force using only the static equilibrium of this model. Furthermore, we extend the conventional gust factor approach to active base isolation to estimate the maximum displacement and maximum control force for active base isolation without the need for numerical simulations. We validate our methods through a series of numerical examples, incorporating key parameters such as feedback gain, aspect ratio of building, return period of wind force, and stiffness of isolation. Numerical verifications show that the mean response and mean control force are estimated by the static equilibrium of the proposed equivalent passive model. Moreover, the maximum response and maximum control force can be estimated by the proposed gust factors. Our methods can be applied for feedback control systems using a given feedback gain.

1. Introduction

Passive base isolation has proven to be an influential solution for enhancing the durability of buildings and infrastructure against seismic threats [1–3]. The prevalence of such structures in Japan has seen a remarkable surge following the devastating Great Hanshin earthquake of 1995 [4]. Conventionally, base-isolated structures are applied to low- and midrise buildings, such as those in [5–7], to suppress the absolute acceleration and interstory drift of the superstructure, thereby substantially reducing the likelihood of structural damage during earthquakes. Recent developments in base-isolation structures have also seen the implementation of base isolation in high-rise buildings [8] to prevent damage to the superstructure. However, applying base isolation in high-rise buildings brings about new issues to tackle. As the height of a building increases, so does the wind load that directly impacts the superstructure. Furthermore, the mean component of the along-wind force results in excessive displacement of the isolation layer that cannot be adequately suppressed by adding the damping of the isolation story [9]. Increasing the stiffness of the isolation

layer may seem the most effective solution, but such alterations increase the absolute acceleration response of the structure. Consequently, the combination of active structural control and passive base isolation (active base isolation) emerges as a viable alternative to address these variations between wind and earthquake forces in the proposed structural system [10, 11].

Although the effectiveness of the active base isolation has been shown in many studies, its applications are still few around the world. One reason for this problem may be considered as the complexity involved in designing active base-isolation systems [12]. Estimations of the maximum response and control force of an active structural control system conventionally rely on numerical simulations. However, due to the lengthy duration of wind events and the averaging of several cases to calculate responses of control systems, these simulations are often time consuming. Moreover, designing control systems often uses a trial-and-error process, which adds additional complexity when selecting a controller to fulfill all design requirements. The design of base-isolation buildings with active structural control is thus fraught with significant guesswork, testing, and prolonged simulation times [12]. On the contrary, conventional passive wind-resistant designs widely use the well-developed gust factor approach to estimate the maximum response without the need for numerical simulations [13, 14]. Expanding the gust factor approach to active base isolation could similarly streamline this intricate conventional design.

Kumar et al. and Kohiyama et al. proposed an equivalent passive model of a single-degree-of-freedom (single-DOF) control system that theoretically describes the system dynamics [15, 16]. This equivalent passive model allows for straightforward estimation of the vibration characteristics of control systems to estimate the maximum responses. However, these studies did not consider the maximum control force, a crucial factor for active structural control when selecting a controller. To address this, Sato et al. and Chen et al. devised a control force spectrum using the equivalent passive model to estimate the maximum control force for single-DOF active base-isolation systems subjected to earthquake disturbance [17–19]. Still, these methods only consider earthquake disturbances and cannot be used to estimate the responses and control force of an active structural control system subjected to wind force.

To rectify these issues, Chen et al. applied the gust factor approach to active base-isolated buildings designed by the linear-quadratic regulator (LQR) method to estimate both the maximum response and the control force [20]. However, this previous method still has the following two main issues:

(i) The previous method employs solving an equation, which contains high-dimensional matrices, to calculate the mean control force and response. Therefore, finding the solution to the equation is relatively complex, and the method itself is challenging to comprehend.

(ii) The previous method is only suitable for one specific case of LQR weighting matrices, which are designed exclusively to suppress the maximum response of the isolated story. This limits the scope of application of the method.

This paper proposes a new method, based on the gust factor approach, for multi-DOF lumped-mass models with a given feedback control gain to estimate both the maximum response and maximum control force (Figure 1), thereby eliminating the need for numerical simulations. Initially, we present a methodology for constructing the equivalent passive model of a multi-DOF control system to theoretically delineate the dynamics of the system. Following this, we develop a method to calculate the mean displacement and control force using only the static equilibrium of the constructed equivalent passive model. Furthermore, we propose gust factors for displacement and control force to estimate the maximum response and control force of the control system based on the calculated mean values. Compared with the previous method, the advantages of the method proposed in this paper are given below:

(i) The method proposed in this paper uses only the static equilibrium of the constructed equivalent passive model to compute the mean response and mean control force. It eliminates the need to solve a complex equation with high-dimensional matrices.

(ii) This method does not restrict the selection of LQR weighting matrices, extending its scope of application.

The method proposed in this paper can be used to estimate the maximum control force for feedback control systems. To verify the efficacy of the presented methods, we use numerical examples that incorporate feedback gain, aspect ratio, wind force return period, and isolation natural period as parameters. Through this study, we aim to bring clarity to the challenges of designing active base isolation and provide a reliable, practical solution.

2. Mathematical Model and Wind Force

This section shows the mathematical model and the along-wind force utilized in this paper.

2.1. Mathematical Model. This paper considers a base-isolated steel base-isolated building (refer to Figure 2(a)). We assume that the height of the superstructure H is 100 meters, and the density of the superstructure ρ_s is 175 kg/m^3 (refer to the density of high-rise steel structures). The first natural period of the superstructure $T_{s,m1}$ is defined by the following equation (21):

$$T_{s,m1} = 0.02H = 0.02 \times 100 = 2\,s. \tag{1}$$

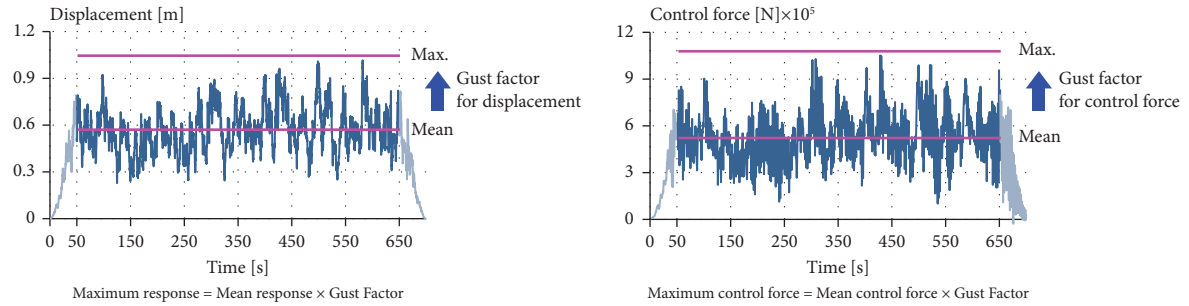

Figure 1: Gust factor approach for active base isolation.

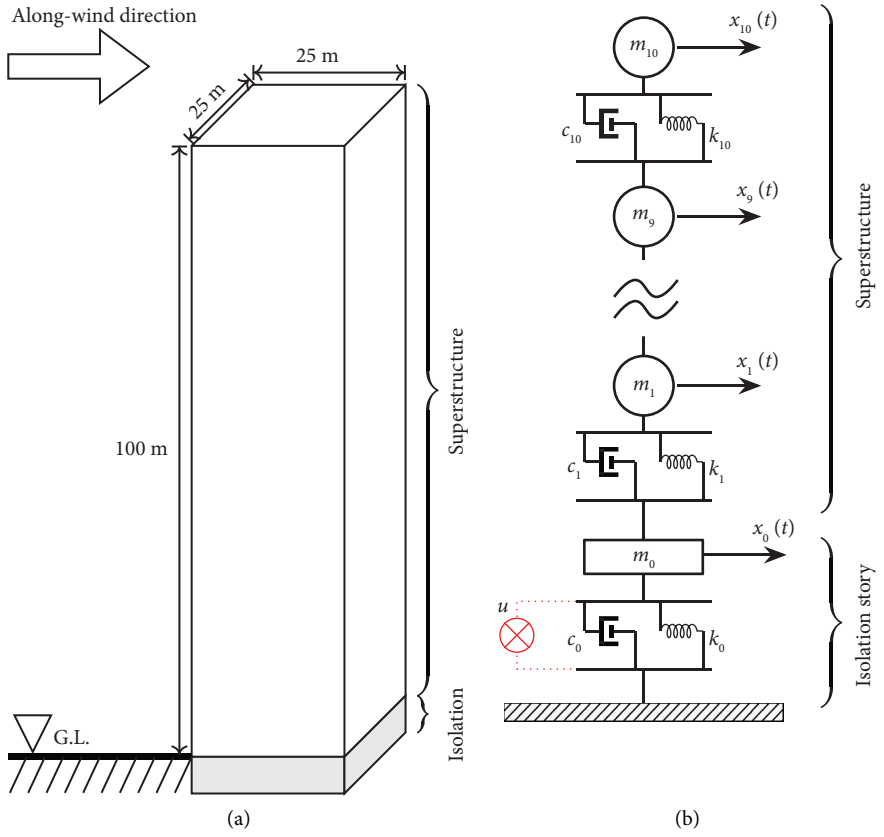

Figure 2: Buildings and mathematic model. (a) Buildings and (b) mathematic model.

The damping ratio for the superstructure's first natural period is assumed as 0.02 (no additional damper is installed in the superstructure). As our method is proposed for a shear-frame model, the superstructure of the building is represented as a 10-DOF lumped-mass shear model. Note that 1 DOF of the superstructure represents a couple of floors.

An isolation story (1 DOF) is positioned beneath the superstructure, and the control device is situated at the isolation story. The base-isolation's mass per unit area ρ_0 is 2551 kg/m^2 [21]. The isolation layer of the model contains a natural multilayer rubber-bearing, linear viscous dampers, and actuators. The isolated natural period (the period that assumes that the superstructure is rigid) T_0 is 4 s, and the damping ratio for the isolated period natural ζ_0 is 0.05. The control force is generated by the actuators.

Consequently, the models have 11 DOFs (see Figure 2(b)). Table 1 presents the parameters of the mathematical model.

The mass, stiffness, and damping coefficient of the superstructure of the model are defined by the following equations (22):

Table 1: Parameter of the mathematic model.

	Parameter	Symbol	Value
Superstructure	Height	H_s	100 m
	Width	B_s	25 m
	Depth	D_s	25 m
	DOF	—	10
	Height of each story	h_i	10 m
	Density	ρ_s	175 kg/m^3
	1st natural period	$T_{s,m1}$	2 s
	1st damping ratio	$\zeta_{s,m1}$	0.02
Isolation	Width	B_0	25 m
	Depth	D_0	25 m
	DOF	—	1
	Mass per unit area	ρ_0	2551 kg/m^2
	Isolated period	T_0	4 s
	Isolated damping ratio	ζ_0	0.05

$$m_i = \rho_s B_s D_s h_i, \quad i = 1 \sim 10, \tag{2a}$$

$$k_i = \begin{cases} \dfrac{\omega_{s,m1}^2 m_1 \phi_{s,1} + k_2\left(\phi_{s,2} - \phi_{s,1}\right)}{\phi_{s,1}}, & i = 1, \\ \dfrac{\omega_{s,m1}^2 m_i \phi_{s,i} + k_{i+1}\left(\phi_{s,i+1} - \phi_{s,i}\right)}{\phi_{s,i} - \phi_{s,i-1}}, & i = 2 \sim 9, \\ \dfrac{\omega_{s,m1}^2 m_{10} \phi_{s,10}}{\phi_{s,10} - \phi_{s,9}}, & i = 10, \end{cases} \tag{2b}$$

$$c_i = \frac{2\zeta_{s,m1}}{\omega_{s,m1}} k_i, \quad i = 1 \sim 10, \tag{2c}$$

where $\omega_{s,m1} = 2\pi/T_{s,m1}$ represents the superstructure's 1st natural angular frequency, and $\phi_{s,i}$ is the i th-story amplitude of the first mode of the superstructure. This study uses a straight-line mode for the first mode of the superstructure as follows:

$$\phi_{s,i} = i. \tag{3}$$

The mass, stiffness, and damping ratio of the isolation layer are determined by the subsequent equations:

$$\begin{aligned} m_0 &= \rho_0 B_0 D_0, \\ k_0 &= \frac{4\pi^2}{T_0^2} \sum_{i=0}^{10} m_i, \\ c_0 &= \frac{4\pi\zeta_0}{T_0} \sum_{i=0}^{10} m_i, \end{aligned} \tag{4}$$

where ϕ_0 is the mass per unit area of the base-isolated layer, T_0 and ζ_0 represent the natural period and damping ratio assuming that the superstructure is a rigid body (isolated period and isolated damping ratio).

The dynamics of the models are described by the following equation:

$$\mathbf{M}\mathbf{x}(t) + \mathbf{C}\dot{\mathbf{x}}(t) + \mathbf{K}\mathbf{x}(t) = \mathbf{E}_\mathbf{f}\mathbf{f}(t) - \mathbf{E}_\mathbf{u}u(t), \tag{5}$$

in which

$$\mathbf{M} = \begin{bmatrix} m_0 & & & \\ & m_1 & & \\ & & \ddots & \\ & & & m_{10} \end{bmatrix}, \tag{6a}$$

$$\mathbf{K} = \begin{bmatrix} k_0 + k_1 & -k_1 & & \\ -k_1 & k_1 + k_2 & -k_2 & \\ & -k_2 & \ddots & \\ & & -k_{10} & k_{10} \end{bmatrix}, \tag{6b}$$

$$\mathbf{C} = \begin{bmatrix} c_0 + c_1 & -c_1 & & \\ -c_1 & c_1 + c_2 & -c_2 & \\ & -c_2 & \ddots & \\ & & -c_{10} & c_{10} \end{bmatrix}, \tag{6c}$$

$$\mathbf{x}(t) = \begin{bmatrix} x_0(t) \\ x_1(t) \\ \vdots \\ x_{10}(t) \end{bmatrix}, \quad \mathbf{f}(t) = \begin{bmatrix} 0 \\ f_1(t) \\ \vdots \\ f_{10}(t) \end{bmatrix}, \tag{6d}$$

$$\mathbf{E}_\mathbf{f} = \mathbf{I}, \tag{6e}$$

$$\mathbf{E}_\mathbf{u} = \begin{bmatrix} 1 & 0 & \cdots & 0 \end{bmatrix}^T, \tag{6f}$$

where $\mathbf{M}$, $\mathbf{K}$, and $\mathbf{C}$ represent the mass, stiffness, and damping matrices of the model, respectively, $\mathbf{x}(t)$, $\dot{\mathbf{x}}(t)$, and $\mathbf{x}(t)$ are the displacement, velocity, and acceleration vectors, respectively, $\mathbf{f}$ is the wind force vector, $x_i(t)$ and $f_i(t)$ are the displacement and wind force of the i th story (0th story indicates the isolation story), respectively, $u(t)$ is the control

force, $\mathbf{E_f}$ and $\mathbf{E_u}$ are the input matrices for $\mathbf{f}(t)$ and $u(t)$, respectively, and $\mathbf{I}$ is a unit matrix.

2.2. Wind Force. This study utilizes the along-wind force, as determined by wind tunnel test data [23, 24]. The parameters of the wind tunnel test are presented in Table 2. The airflow in the test is determined by referencing the building design code in Japan [25]. The parameters of the wind force for simulation are displayed in Table 3.

This paper employs 30 cases of 10-minute wind waves to conduct numerical simulations. It should be noted that the wind data include envelopes at the first and last 50 seconds to minimize the influence of transient response (refer to Figure 3), and the responses are computed by the ensemble average of 30 cases using only the values from 50 seconds to 650 seconds. Figure 4 illustrates the power spectral density (PSD) of the wind force of the 10th story (ensemble average of 30 cases). Figure 5 portrays the mean and maximum wind force exerted on each story of the model (ensemble average of 30 cases).

3. Control System

Semiactive control requires using a small external energy to generate significant control force by dynamically altering the structural damping coefficient or stiffness and is inherently stable. Its effectiveness has been validated via analytical and experimental studies [26–28]. However, semiactive control devices usually have a relatively small control force and cannot add or remove energy to the structure. Because suppressing the isolation story's displacement for a high-rise building requires extremely control force, this study uses active structural control strategy.

This section constructs the control system using the linear quadratic regulator (LQR) method, one of the standard methods for active structural control [29–31]. Subsequently, it shows four cases of LQR weighting matrices, intended for numerical examples.

3.1. Construction of the Control System. The state-space representation of (5) is as follows:

$$\dot{\mathbf{z}}(t) = \mathbf{A}\mathbf{z}(t) + \mathbf{B_f}\mathbf{f}(t) - \mathbf{B_u}u(t), \tag{7}$$

where

$$\mathbf{z}(t) = \left[\mathbf{x}^{\mathrm{T}}(t) \;\; \dot{\mathbf{x}}^{\mathrm{T}}(t)\right]^{\mathrm{T}}, \tag{8a}$$

$$\mathbf{A} = \begin{bmatrix} \mathbf{0} & \mathbf{I} \\ -\mathbf{M}^{-1}\mathbf{K} & -\mathbf{M}^{-1}\mathbf{C} \end{bmatrix}, \tag{8b}$$

$$\mathbf{B_f} = \left[0 \;\cdots\; 0 \;\; \left(\mathbf{M}^{-1}\mathbf{E_f}\right)^{\mathrm{T}}\right]^{\mathrm{T}}, \text{and} \tag{8c}$$

$$\mathbf{B_u} = \left[0 \;\cdots\; 0 \;\; \left(\mathbf{M}^{-1}\mathbf{E_u}\right)^{\mathrm{T}}\right]^{\mathrm{T}}. \tag{8d}$$

Table 2: Parameter of the wind tunnel test.

Parameter	Value
Scale	1/250
Wind velocity	10 m/s
Wind direction angle	0°
Story	8
Sampling frequency	1000 Hz

Table 3: Parameter of wind force for simulation.

Parameter	Value
Return period	500 years
Terrain category	III
Wind direction angle	0°
Wind velocity (top story)	63.8 m/s

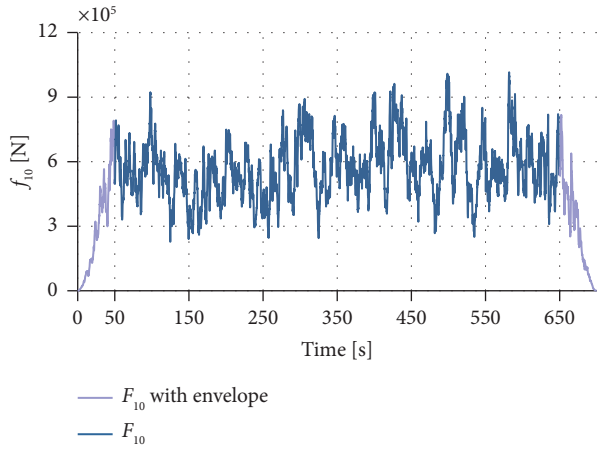

Figure 3: Wind force of 10th story (1 case).

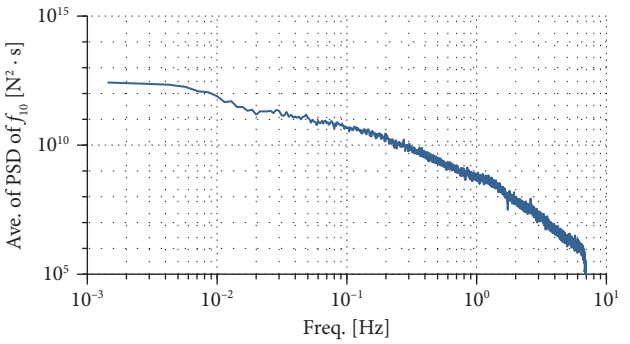

Figure 4: PSD of f_{10} (ensemble average of 30 cases).

Here, $\mathbf{z}(t)$ is the state vector, $\mathbf{A}$ is the system matrix, and $\mathbf{B_f}$ and $\mathbf{B_u}$ are the input gain for $\mathbf{f}(t)$ and $u(t)$, respectively. The study uses the subsequent feedback control law:

$$u(t) = \mathbf{K_p}\mathbf{z}(t), \tag{9}$$

where $\mathbf{K_p}$ is the feedback gain.

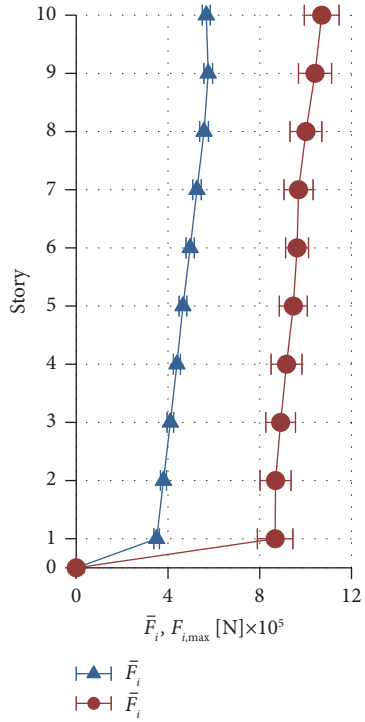

FIGURE 5: Story wind force (ensemble average of 30 cases with standard deviation).

Note that $\mathbf{K_P}$ is a horizontal vector with 22 entries. The first 11 entries are the displacement-feedback gain $\mathbf{K_{PD}}$, and the last 11 entries are the velocity-feedback gain $\mathbf{K_{PV}}$. Therefore, equation (9) can be represented by the following equation:

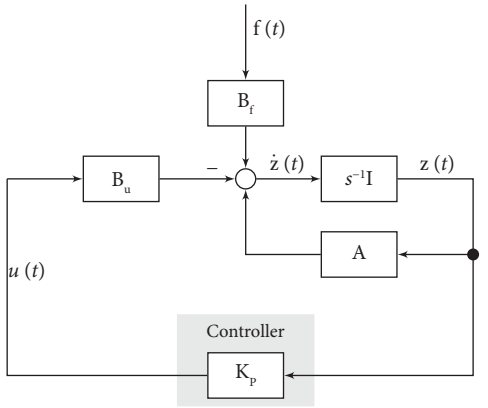

FIGURE 6: Block diagram of the control system.

$$u(t) = \left[\mathbf{K_{PD}} \;\; \mathbf{K_{PV}}\right]\left[\mathbf{x}^{\mathrm{T}}(t) \;\; \dot{\mathbf{x}}^{\mathrm{T}}(t)\right]^{\mathrm{T}} = \mathbf{K_{PD}}\mathbf{x}(t) + \mathbf{K_{PV}}\dot{\mathbf{x}}(t). \tag{10}$$

Figure 6 illustrates the block diagram of the control system utilized in this paper.

This study employs the LQR method to design the feedback gain, $\mathbf{K_P}$. The LQR method minimizes J in the subsequent cost funtion for a control system subjected to an impulsive excitation [32]:

$$J = \int_0^\infty \left[\mathbf{z}^{\mathrm{T}}(t)\mathbf{Q}\mathbf{z}(t) + u^{\mathrm{T}}(t)R\mathrm{u}(t)\right]\mathrm{d}t. \tag{11}$$

where $\mathbf{Q} \geq \mathbf{0}$ and $R > 0$ are the weighting matrices for the state and control force, respectively. The following weighting matrices are utilized in this paper:

$$\mathbf{Q} = 10^{\beta}\mathrm{diag}.\left\{ q_{\mathrm{D0}} \;\; q_{\mathrm{D1}} \;\; \cdots \;\; q_{\mathrm{D10}} \;\middle|\; q_{\mathrm{V0}} \;\; q_{\mathrm{V1}} \;\; \cdots \;\; q_{\mathrm{V10}} \right\} \text{ and} \tag{12a}$$

$$R = 1, \tag{12b}$$

where q_{Di} and q_{Vi} are the diagonal weighting entries of $\mathbf{Q}$ for displacement and velocity, respectively, and β is the weighting coefficient of $\mathbf{Q}$. The weighting coefficient β determines the relative weight of the cost function (11) in the optimization problem. Note that increasing the value of β results in an enhancement in active control effect. Conversely, if β is sufficiently small, the system will have little or no active control effect (similar to a passive-controlled structure).

Upon solving (11), the feedback gain $\mathbf{K_P}$ is determined as the following equation:

$$\mathbf{K_P} = R^{-1}\mathbf{B_u^{\mathrm{T}}}\mathbf{P}, \tag{13}$$

where $\mathbf{P}$ (≥ 0) is the solution of the following algebraic Riccati equation (33):

$$\mathbf{A}^T\mathbf{P} + \mathbf{P}\mathbf{A} - \mathbf{P}\mathbf{B_u}R^{-1}\mathbf{B_u^{\mathrm{T}}}\mathbf{P} + \mathbf{Q} = \mathbf{0}. \tag{14}$$

Note that the solution of the algebraic Riccati equation $\mathbf{P}$ in equation (14) and the feedback gain $\mathbf{K_P}$ are invariant with time. Equation (14) yields an optimal solution only for impulsive excitation to adjust the vibration characteristics. The LQR method cannot guarantee an optimal solution for the actual excitation term, as noted in [34].

3.2. Selecting of Weighting Matrices. The methods proposed in this paper uses a given feedback gain to estimate the maximum response and control force. Therefore, this paper uses four cases of the LQR weighting matrices (Table 4) as numerical examples to validate the effectiveness of the estimation method. This section assigns weight entries for displacement only, setting all weight entries for velocity to

Table 4: Selection of weighting matrices ($q_{V,i} = 0$).

Story	Case A		Case B		Case C		Case D	
i	$q_{D,i}$	$q_{V,i}$	$q_{D,i}$	$q_{V,i}$	$q_{D,i}$	$q_{V,i}$	$q_{D,i}$	$q_{V,i}$
0	1	0	0	0	1	0	1	0
1	0	0	0	0	0	0	1	0
2	0	0	0	0	0	0	1	0
3	0	0	0	0	0	0	1	0
4	0	0	0	0	0	0	1	0
5	0	0	0	0	0	0	1	0
6	0	0	0	0	0	0	1	0
7	0	0	0	0	0	0	1	0
8	0	0	0	0	0	0	1	0
9	0	0	0	0	0	0	1	0
10	0	0	1	0	1	0	1	0

0 to suppress the displacement response. Furthermore, Appendix A provides validations for the cases that $q_{V,i} \neq 0$ and compares the control performance with the cases used in this section.

4. Equivalent Model and Estimation of Mean Response

This section introduces a method to construct an equivalent passive model for a multi-DOF control system. Subsequently, we propose a method for estimating the mean response and mean control force, solely using the static equilibrium of the constructed equivalent passive model.

4.1. Construction of Equivalent Model. In this study, the equivalent model of an active system is defined as a model that generates the same responses as the original active system when subjected to the same disturbance [15, 16].

Substituting the control law, given in (9), into the vibration equation, (5), results in the following equation:

$$\mathbf{M}\ddot{\mathbf{x}}(t) + \mathbf{C}\dot{\mathbf{x}}(t) + \mathbf{K}\mathbf{x}(t) = \mathbf{E}_\mathbf{F}\mathbf{f}(t) - \mathbf{E}_\mathbf{u}\left[\mathbf{K}_\mathbf{PD}\mathbf{x}(t) + \mathbf{K}_\mathbf{PV}\dot{\mathbf{x}}(t)\right]. \tag{15}$$

Representing (15) yields the dynamics of the equivalent model as follows:

$$\mathbf{M}\ddot{\mathbf{x}}(t) + \mathbf{C}_\mathbf{eq}\dot{\mathbf{x}}(t) + \mathbf{K}_\mathbf{eq}\mathbf{x}(t) = \mathbf{E}_\mathbf{f}\mathbf{f}(t), \tag{16}$$

where $\mathbf{K}_\mathbf{eq}$ and $\mathbf{C}_\mathbf{eq}$ are the stiffness matrix and damping matrix of the equivalent model, respectively (equivalent stiffness matrix and equivalent damping matrix). The definitions of $\mathbf{K}_\mathbf{eq}$ and $\mathbf{C}_\mathbf{eq}$ are shown in the subsequent equations:

$$\mathbf{K}_\mathbf{eq} = \mathbf{K} + \mathbf{E}_\mathbf{u}\mathbf{K}_\mathbf{PD} \text{ and} \tag{17a}$$

$$\mathbf{C}_\mathbf{eq} = \mathbf{C} + \mathbf{E}_\mathbf{u}\mathbf{K}_\mathbf{PV}. \tag{17b}$$

Using equation (16), the vibration characteristics of a multi-DOFs active control system can be represented as a passive model. Note that the equivalent stiffness matrix and equivalent damping matrix, $\mathbf{K}_\mathbf{eq}$ and $\mathbf{C}_\mathbf{eq}$, are nonsymmetric. Also, the state-space equation of the equivalent model is

$$\dot{\mathbf{z}}(t) = \mathbf{A}_\mathbf{eq}\mathbf{z}(t) + \mathbf{B}_\mathbf{f}\mathbf{f}(t), \tag{18}$$

where $\mathbf{A}_\mathbf{eq}$ is the system matrix of the equivalent model, defined by the following equation:

$$\begin{aligned}\mathbf{A}_\mathbf{eq} &= \mathbf{A} + \mathbf{B}_\mathbf{u}\mathbf{K}_\mathbf{P} \\ &= \begin{bmatrix} \mathbf{0} & \mathbf{I} \\ -\mathbf{M}^{-1}\mathbf{K}_\mathbf{eq} & -\mathbf{M}^{-1}\mathbf{C}_\mathbf{eq} \end{bmatrix}.\end{aligned} \tag{19}$$

4.2. Estimation of Mean Displacement and Mean Control Force. By utilizing the static equilibrium of equation (16), the mean displacement response of the system can be estimated as follows:

$$\bar{\mathbf{x}} = \mathbf{K}_\mathbf{eq}^{-1}\mathbf{E}_\mathbf{f}\bar{\mathbf{f}}, \tag{20}$$

where $\bar{\mathbf{f}}$ is the mean-wind-force vector.

Furthermore, from (9), the mean control force $\bar{u}$ is

$$\bar{u} = \mathbf{K}_\mathbf{PD}\bar{\mathbf{x}} + \mathbf{K}_\mathbf{PD}\bar{\dot{\mathbf{x}}}, \tag{21}$$

where $\bar{\mathbf{x}}$ and $\bar{\dot{\mathbf{x}}}$ are the mean-displacement vector and mean-velocity vector, respectively.

As the velocity response of a control system does not contain a mean component [35], substituting (20) into (21) yields

$$\bar{u} = \mathbf{K}_\mathbf{PD}\mathbf{K}_\mathbf{eq}^{-1}\mathbf{E}_\mathbf{f}\bar{\mathbf{f}}. \tag{22}$$

Using equations (20) and (22), the mean displacement and mean control force are estimated by the static equilibrium of the constructed equivalent passive model. From (20) and (22), the following results are obtained:

(i) Using the constructed equivalent passive model, the mean displacement and mean control force are estimated only by using the static equilibrium without the need for numerical simulations.
(ii) Equations (20) and (22) contain an inverse of the equivalent stiffness matrix $\mathbf{K}_\mathbf{eq}$ and hence there are no analytical solutions for a system with more than 2 DOFs.

Compared to the previous method, which requires solving an equation containing high-dimensional matrices [20], the method proposed in this paper ((20) and (22)) only requires the inverse matrix of the equivalent stiffness matrix

$\mathbf{K_{eq}}$. As a result, the proposed method offers a more efficient way to estimate the mean displacement and mean control force of the system without the need for numerical simulations.

5. Gust Factor for the Active Control System

The gust factor approach, as applied to the along-wind direction, is a widely-used well-developed method for estimating the maximum response of the structure without the need for complex numerical simulations or wind tunnel tests. Section 5.1 extends the gust factor for displacement to active control systems to estimate the maximum displacement response. Furthermore, Section 5.2 devises a new gust factor to estimate the maximum control force.

5.1. Gust Factor for Displacement. This study uses the subsequent equation to estimate the gust factor of displacement, referring to AIJ Recommendations for Loads on Buildings [25].

$$G_D = 1 + g_{\mathrm{D}} \frac{C_{\mathrm{g}}'}{C_{\mathrm{g}}} \sqrt{1 + \phi_{\mathrm{D}}^2 R_{\mathrm{D}}}, \tag{23}$$

where

$$g_D = \sqrt{2\ln(600 v_{\mathrm{D}})} + 1.2, \tag{24a}$$

$$C_{\mathrm{g}}' = 2 I_H \frac{0.49 - 0.14\alpha}{\left[1 + \left(0.63\left(\sqrt{BH}/L_H\right)^{0.56}/(H/B)^{\kappa}\right)\right]} \begin{cases} \kappa = 0.07, & \left(\frac{H}{B} \geq 1\right), \\ \kappa = 0.15, & \left(\frac{H}{B} < 1\right). \end{cases} \tag{24b}$$

$$C_{\mathrm{g}} = \frac{1}{3 + 3\alpha} + \frac{1}{6}, \tag{24c}$$

$$\phi_{\mathrm{D}} = \frac{3}{2 + \beta} \frac{M_{D1}}{M_D} \lambda, \tag{24d}$$

$$R_{\mathrm{D}} = \frac{\pi F_D}{4\zeta_{m1,\mathrm{eq}}}, \tag{24e}$$

$$v_{\mathrm{D}} = f_{m1,\mathrm{eq}} \sqrt{\frac{R_D}{1 + R_D}}, \tag{24f}$$

$$F_{\mathrm{D}} = \frac{I_H^2 F S_{\mathrm{D}} (0.57 - 0.35\alpha + 2R\sqrt{0.053 - 0.042\alpha})}{C_{\mathrm{g}}'^2}, \tag{24g}$$

$$R = \frac{1}{1 + 20 + \left(f_{m1,\mathrm{eq}} B/U_H\right)}, \tag{24h}$$

$$F = \frac{4\left(f_{m1,\mathrm{eq}} L_H/U_H\right)}{\left[1 + 71\left(f_{m1,\mathrm{eq}} L_H/U_H\right)^2\right]^{5/6}}, \tag{24i}$$

$$S_{\mathrm{D}} = \frac{0.9}{\left[1 + 6\left(f_{m1,\mathrm{eq}} H'/U_H\right)^2\right]^{0.5} \left(1 + 3\left(f_{m1,\mathrm{eq}} B/U_H\right)\right)}, \tag{24j}$$

$$\lambda = 1 - 0.4\ln\beta, \tag{24k}$$

$$M_D = \int_0^H m(h)\mu^2(h)\mathrm{d}h, \text{ and} \tag{24l}$$

$$\mu(h) = \left(\frac{h}{H}\right)^{\beta}. \tag{24m}$$

The variables are defined as follows: g_D: peak factor of along-wind vibration, C_g: overturning moment coefficient in along-wind direction, C_g': RMS overturning moment coefficient in along-wind direction, ϕ_D: mode shape correction factor, R_D: resonance factor for along-wind vibration, ν_D (Hz): level crossing rate, α: exponent of the power law for wind speed profile, I_H: turbulence intensity at reference height given by equation (25), B (m): building width, L_H (m): turbulence scale at reference height given by equation (28), F_D: along-wind force spectral factor, $\zeta_{m1,eq}$: damping ratio for the 1st mode of the equivalent model, $f_{m1,eq}$ (Hz): natural frequency for the 1st mode of the equivalent model, F: wind force spectrum factor, S_D: size effect factor, R: correlation coefficient between wind pressures on the windward and leeward faces, U_H (m/s): design wind velocity (see Table 3), β: exponent of the power law for the first translational vibration mode in the along-wind direction defined in equation (29), M_D (kg): generalized mass of building for along-wind vibration, M_{D1} (kg): generalized mass of building for along-wind vibration calculated based on $\beta = 1$, λ: mode correction factor of general wind force, $m(h)$ (kg/m): mass per unit height at h m, and $\mu(h)$: 1st mode shape of building in each direction.

Note that $f_{m1,eq}$ and $\zeta_{m1,eq}$ use the 1st natural frequency and 1st damping ratio of the equivalent model (see Figure 7).

The turbulence intensity I_H is defined according to the conditions of the construction site as

$$I_H = I_{rH} E_{gI}, \tag{25}$$

where I_{rH} is the turbulence intensity at height H for each terrain category defined in equation (26), and E_{gI} is the topography factor defined in equation (27).

$$I_{rH} = \begin{cases} 0.1\left(\dfrac{H}{H_G}\right)^{-\alpha-0.05}, & H_b < H \le H_G, \\ 0.1\left(\dfrac{H_b}{H_G}\right)^{-\alpha-0.05}, & H \le H_b, \end{cases} \tag{26}$$

where H_b, H_G, and α are the parameters of the exposure factor as defined in Table 5.

The topography factor for the turbulence intensity is defined as follows:

$$E_{gI} = \frac{E_I}{E_g}, \tag{27}$$

where E_I is the topography factor for the standard deviation of the fluctuating wind speed; E_g is the topography factor. This paper does not consider topography factors $E_I = E_g = 1$.

The turbulence scale L_H is defined according to the terrain category of the construction site as

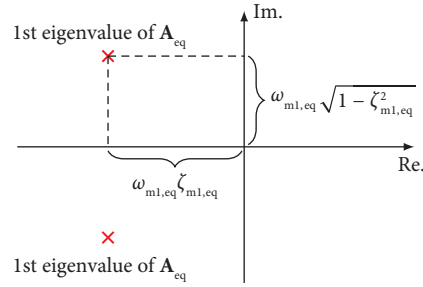

Figure 7: Natural frequency and the damping ratio of 1st mode.

Table 5: Parameters of the exposure factor [25].

Flat terrain categories	I	II	III	IV	V
H_b	3	5	10	20	30
H_G	250	350	450	550	650
α	0.10	0.15	0.20	0.27	0.35

$$L_H = \begin{cases} 100\left(\dfrac{H}{30}\right)^{0.05}, & H_b < H \le H_G, \\ 100\left(\dfrac{H_b}{30}\right)^{0.05}, & H \le H_b. \end{cases} \tag{28}$$

The value of the exponent of the power law for the first translational vibration mode in the along-wind direction, β, is approximated by

$$\beta = 0.51\mu_0^2 - 1.5\mu_0 + 0.99, \tag{29}$$

where μ_0 is the mode displacement at the PBI story (Figure 8).

5.2. Gust Factor for Control Force. The definition of the gust factor for control force G_u is given as follows:

$$G_u = \frac{u_{max}}{\bar{u}}, \tag{30}$$

where u_{max} and $\bar{u}$ are the maximum control force and mean control force, respectively. From the control law, (9), the maximum control force, u_{max}, and mean control force, $\bar{u}$, are given in the following:

$$\bar{u} = \mathbf{K_{PD}}\bar{\mathbf{x}} + \mathbf{K_{PV}}\dot{\bar{\mathbf{x}}} = \mathbf{K_{PD}}\bar{\mathbf{x}}, \tag{31a}$$

$$u_{max} = \max\{\mathbf{K_{PD}}\mathbf{x}(t) + \mathbf{K_{PV}}\dot{\mathbf{x}}(t)\}. \tag{31b}$$

Due to the phase difference between displacement response and velocity response, the maximum value of displacement and velocity usually do not occur simultaneously. Therefore, this study employs the square root of the sum of

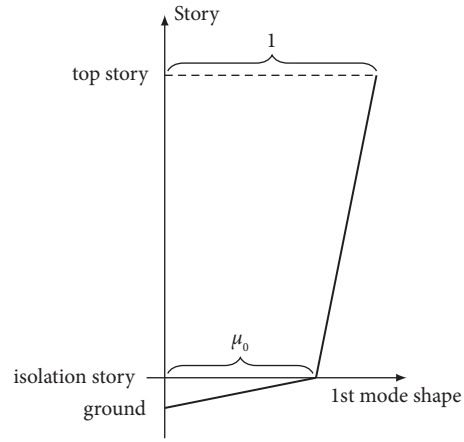

Figure 8: Mode displacement at isolation story μ_0.

squares (SRSSs) to estimate the maximum control force as follows:

$$u_{\max} = \sqrt{\max\left\{\mathbf{K_{PD}x}(t)\right\}^2 + \max\left\{\mathbf{K_{PV}}\dot{\mathbf{x}}(t)\right\}^2}. \tag{32}$$

Given that the 1st mode is dominant for wind-induced vibration, the following assumption is used:

$$\begin{aligned}\bar{u} &= \mathbf{K_{PD}}\bar{\mathbf{x}} \\ &= \bar{x}_0\mathbf{K_{PD}}\boldsymbol{\Phi}_{\mathbf{m1}},\end{aligned} \tag{33a}$$

$$\begin{aligned}\max\{\mathbf{K_{PD}x}(t)\} &= x_{0\max}\mathbf{K_{PD}}\boldsymbol{\Phi}_{\mathbf{m1}} \\ &= G_D\bar{x}_0\mathbf{K_{PD}}\boldsymbol{\Phi}_{\mathbf{m1}}, \text{and,}\end{aligned} \tag{33b}$$

$$\begin{aligned}\max\left\{\mathbf{K_{PV}}\dot{\mathbf{x}}(t)\right\} &= \dot{x}_{0\max}\mathbf{K_{PV}}\boldsymbol{\Phi}_{\mathbf{m1}} \\ &= \left(x_{0\max} - \bar{x}_0\right)\omega_{\mathrm{m1}}\mathbf{K_{PV}}\boldsymbol{\Phi}_{\mathbf{m1}} \\ &= \left(G_D - 1\right)\bar{x}_0\omega_{\mathrm{m1}}\mathbf{K_{PV}}\boldsymbol{\Phi}_{\mathbf{m1}},\end{aligned} \tag{33c}$$

where Φ_{m1} is the 1st mode vector. Substituting (32) and (33) into (30) yields

$$\begin{aligned}G_u &= \frac{\sqrt{\left(G_D\bar{x}_0\mathbf{K_{PD}}\boldsymbol{\Phi}_{\mathbf{m1}}\right)^2 + \left[\left(G_D - 1\right)\bar{x}_0\omega_{m1}\mathbf{K_{PV}}\boldsymbol{\Phi}_{\mathbf{m1}}\right]^2}}{\bar{x}_0\mathbf{K_{PD}}\boldsymbol{\Phi}_{\mathbf{m1}}} \\ &= \sqrt{\left(\frac{G_D\bar{x}_0\mathbf{K_{PD}}\boldsymbol{\Phi}_{\mathbf{m1}}}{\bar{x}_0\mathbf{K_{PD}}\boldsymbol{\Phi}_{\mathbf{m1}}}\right)^2 + \left[\frac{\left(G_D - 1\right)\bar{x}_0\omega_{m1}\mathbf{K_{PV}}\boldsymbol{\Phi}_{\mathbf{m1}}}{\bar{x}_0\mathbf{K_{PD}}\boldsymbol{\Phi}_{\mathbf{m1}}}\right]^2} \\ &= \sqrt{G_D^2 + G_V^2},\end{aligned} \tag{34}$$

Representing (34) yields

$$G_u = \sqrt{G_D^2 + G_{\mathrm{V}}^2}, \tag{35a}$$

$$G_V = \left(G_D - 1\right)\omega_{m1}\frac{\mathbf{K_{PV}}\boldsymbol{\Phi}_{\mathbf{m1}}}{\mathbf{K_{PD}}\boldsymbol{\Phi}_{\mathbf{m1}}}. \tag{35b}$$

Using (35), the maximum control force can be estimated without the need of numerical simulations.

In addition, Appendix B provides a comparison between the gust factor estimation method for control force presented in this paper, Eq. (35), and the previous method [20].

6. Numerical Verification

Figure 9 shows the comparison of the mean displacement and mean control force between estimations (equations (20) and (22)) and simulation results. From Figure 9, the following observations are made:

(i) The mean displacement and mean control force estimated by the equivalent model match well with the simulation results; thus, the validity of equations (20) and (22) is verified.

(ii) The mean displacement of the isolation story decreases as the weighting coefficient β increases.

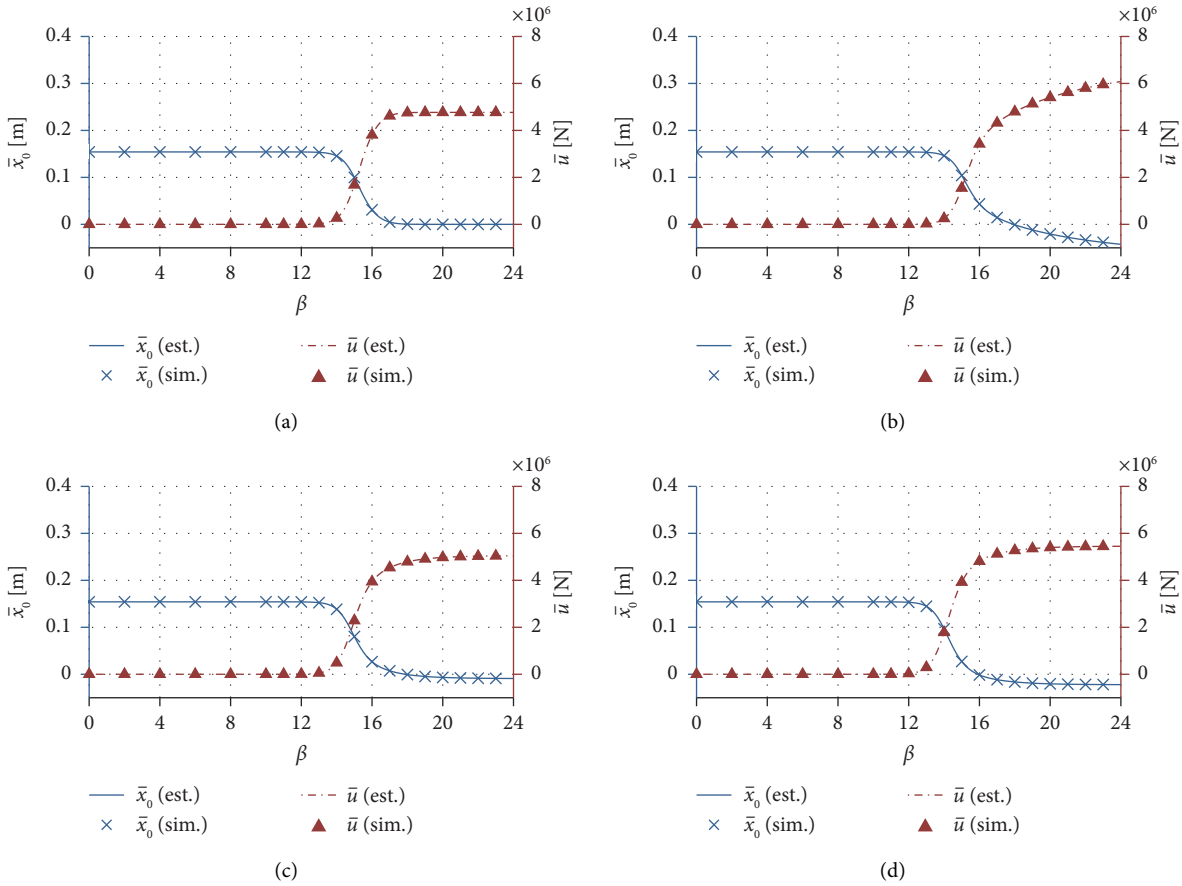

FIGURE 9: Mean displacement and mean control force: estimation vs. simulation result. (a) Case A. (b) Case B. (c) Case C. (d) Case D.

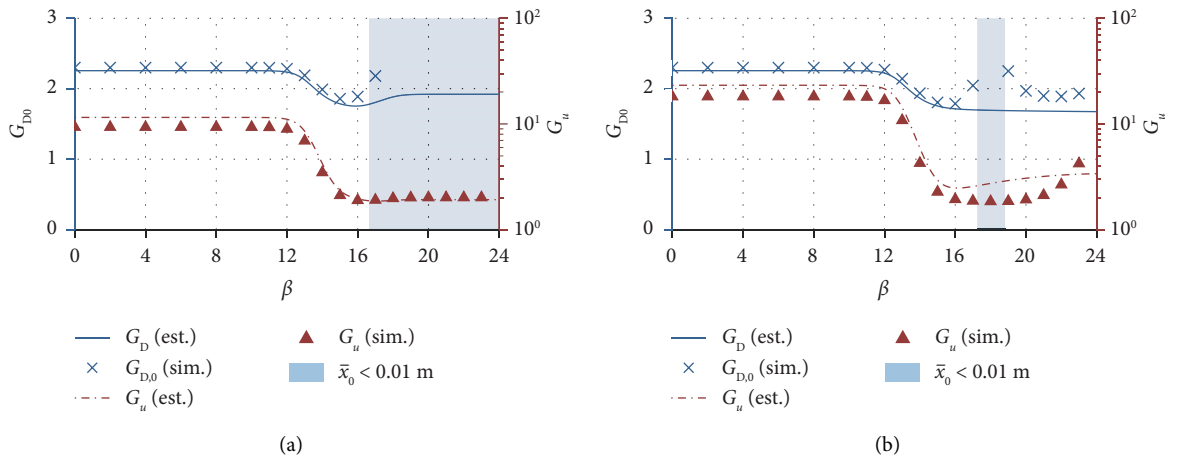

FIGURE 10: Continued.

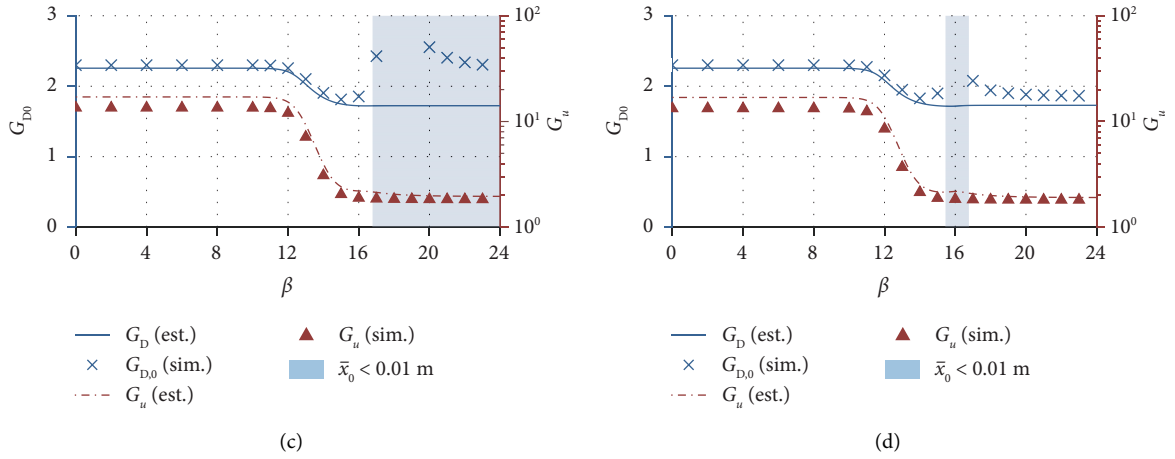

Figure 10: Gust factor for displacement and control force: estimation vs. simulation result. (a) Case A. (b) Case B. (c) Case C. (d) Case D.

Table 6: Selecting of weighting matrices ($q_{V,i} \neq 0$).

i	Case A′		Case B′		Case C′		Case D′	
	$q_{D,i}$	$q_{V,i}$	$q_{D,i}$	$q_{V,i}$	$q_{D,i}$	$q_{V,i}$	$q_{D,i}$	$q_{V,i}$
0	1	1	0	0	1	1	1	1
1	0	0	0	0	0	0	1	1
2	0	0	0	0	0	0	1	1
3	0	0	0	0	0	0	1	1
4	0	0	0	0	0	0	1	1
5	0	0	0	0	0	0	1	1
6	0	0	0	0	0	0	1	1
7	0	0	0	0	0	0	1	1
8	0	0	0	0	0	0	1	1
9	0	0	0	0	0	0	1	1
10	0	0	1	1	1	1	1	1

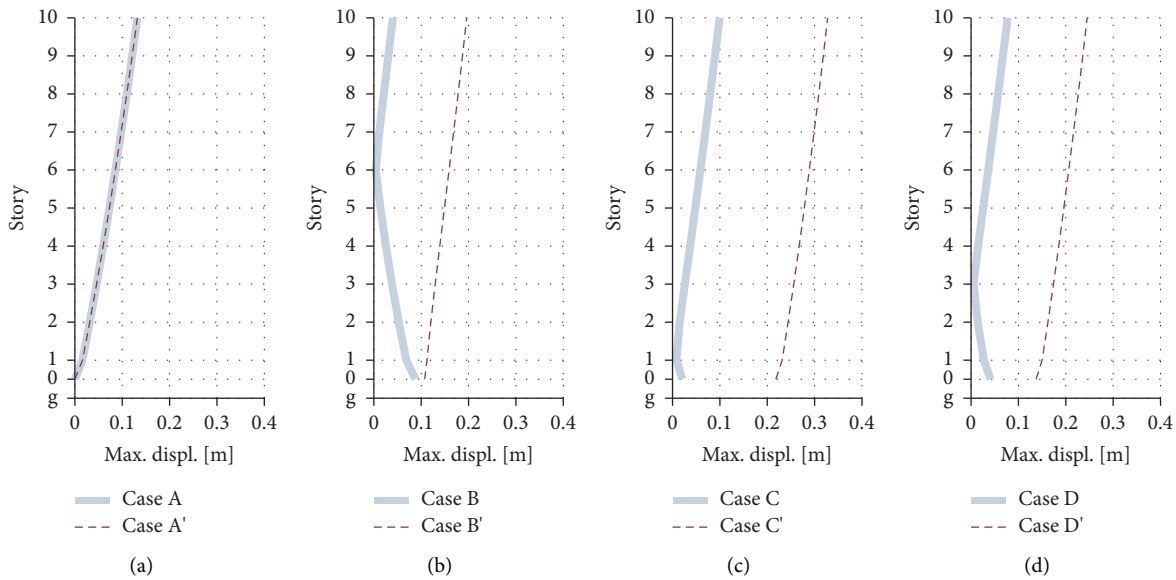

Figure 11: Simulation result of maximum displacement: cases A ~ D vs. cases A′ ~ D′ ($\beta = 24$). (a) Case A vs. case A′. (b) Case B vs. case B′. (c) Case C vs. case C′. (d) Case D vs. case D′.

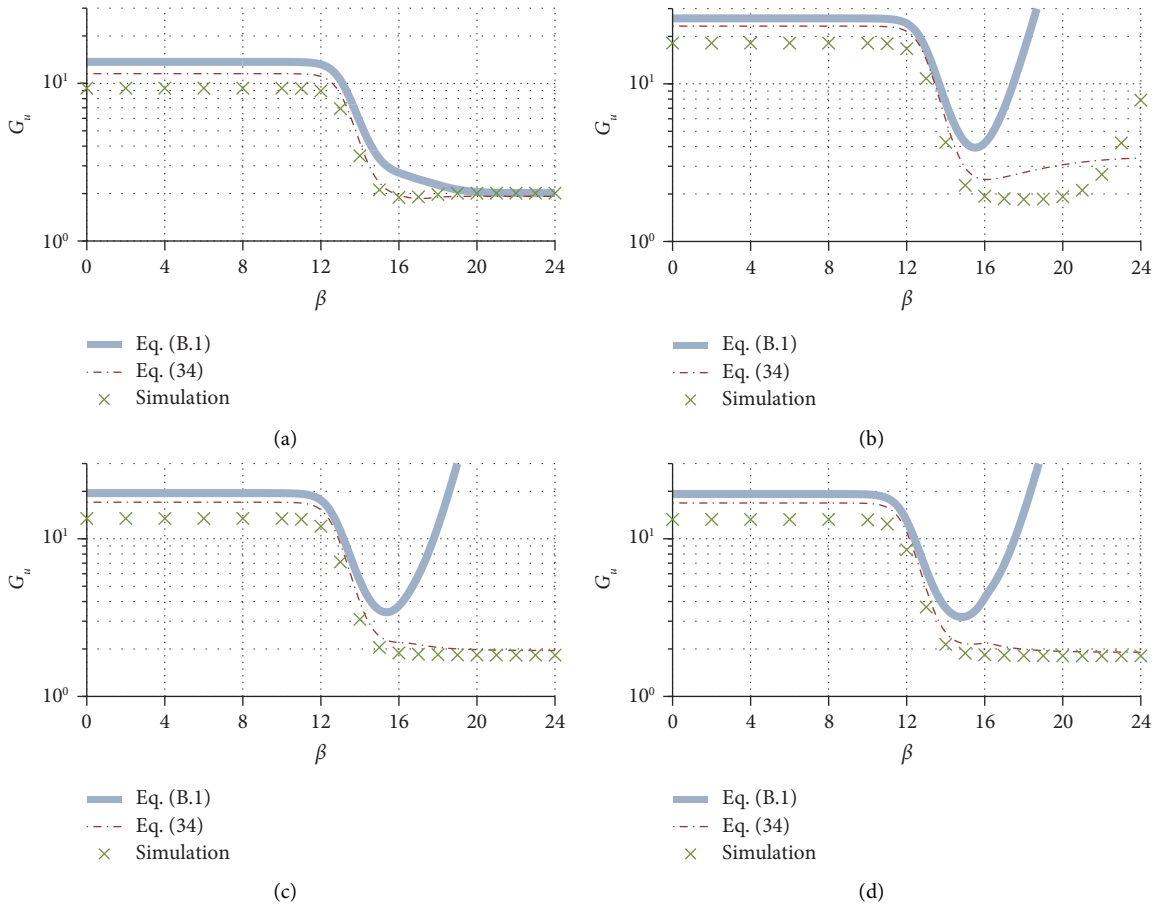

Figure 12: Angle between mean displacement vector and 1st mode vector. (a) Case A. (b) Case B. (c) Case C. (d) Case D.

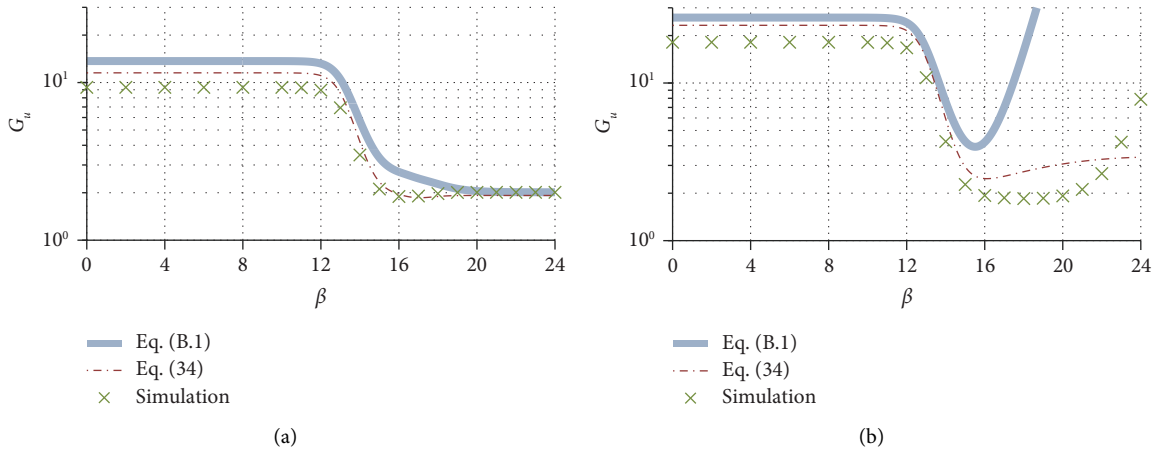

Figure 13: Continued.

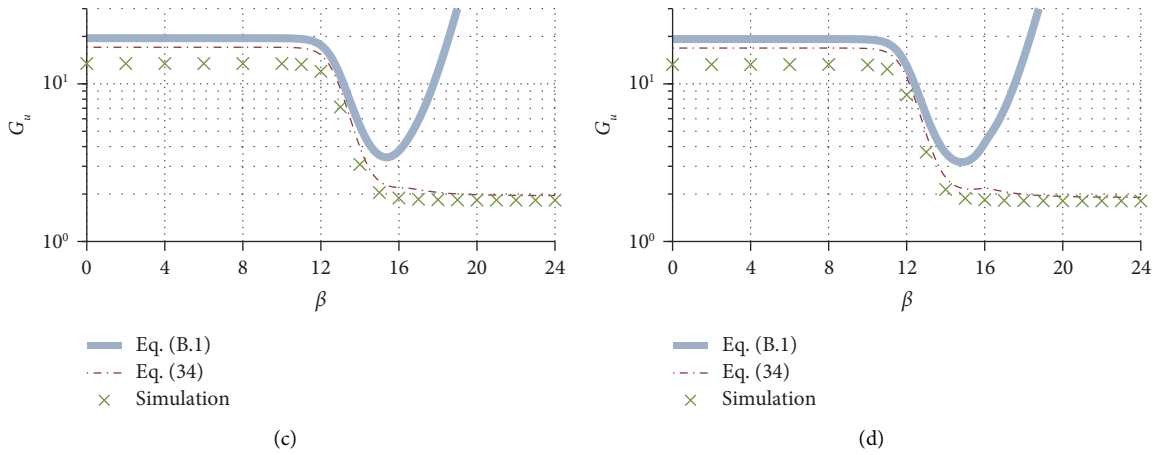

Figure 13: Gust factor for control force: previous method vs. new method. (a) Case A. (b) Case B. (c) Case C. (d) Case D.

Table 7: Parameter of the model used in this section.

Case nos.	Aspect ratio	Return period (year)	Isolated period (s)
1	4	100	3
2	4	100	5
3	4	500	3
4	4	500	5
5	5	100	3
6	5	100	5
7	5	500	3
8	5	500	5

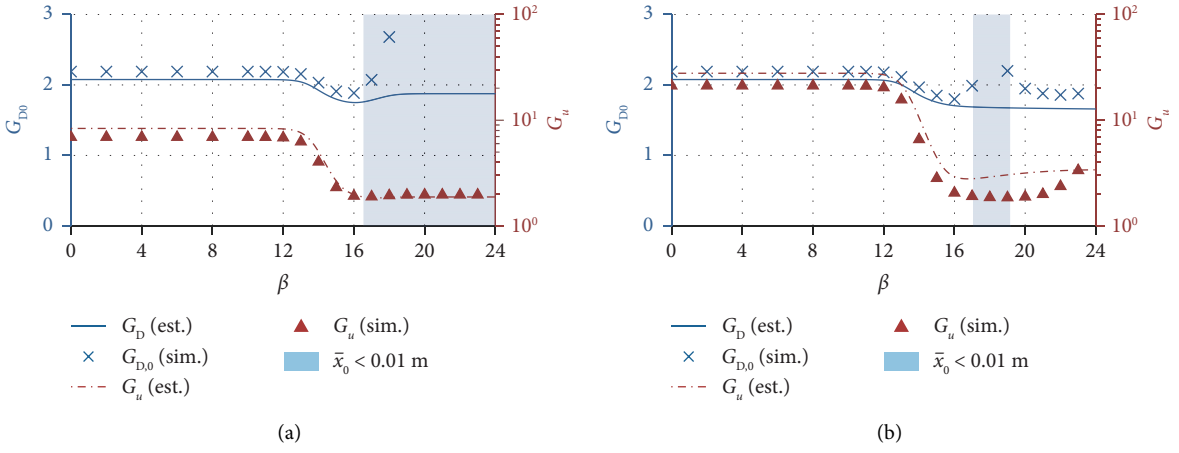

Figure 14: Continued.

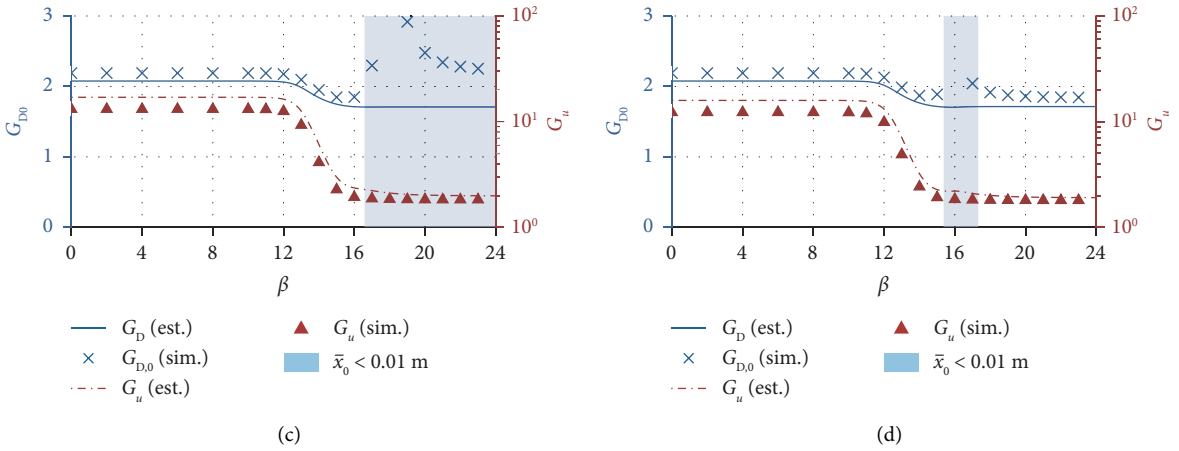

FIGURE 14: Gust factor: estimation vs. simulation result (aspect ratio: 4, return period: 100-year, isolated period: 3 s). (a) Case A. (b) Case B. (c) Case C. (d) Case D.

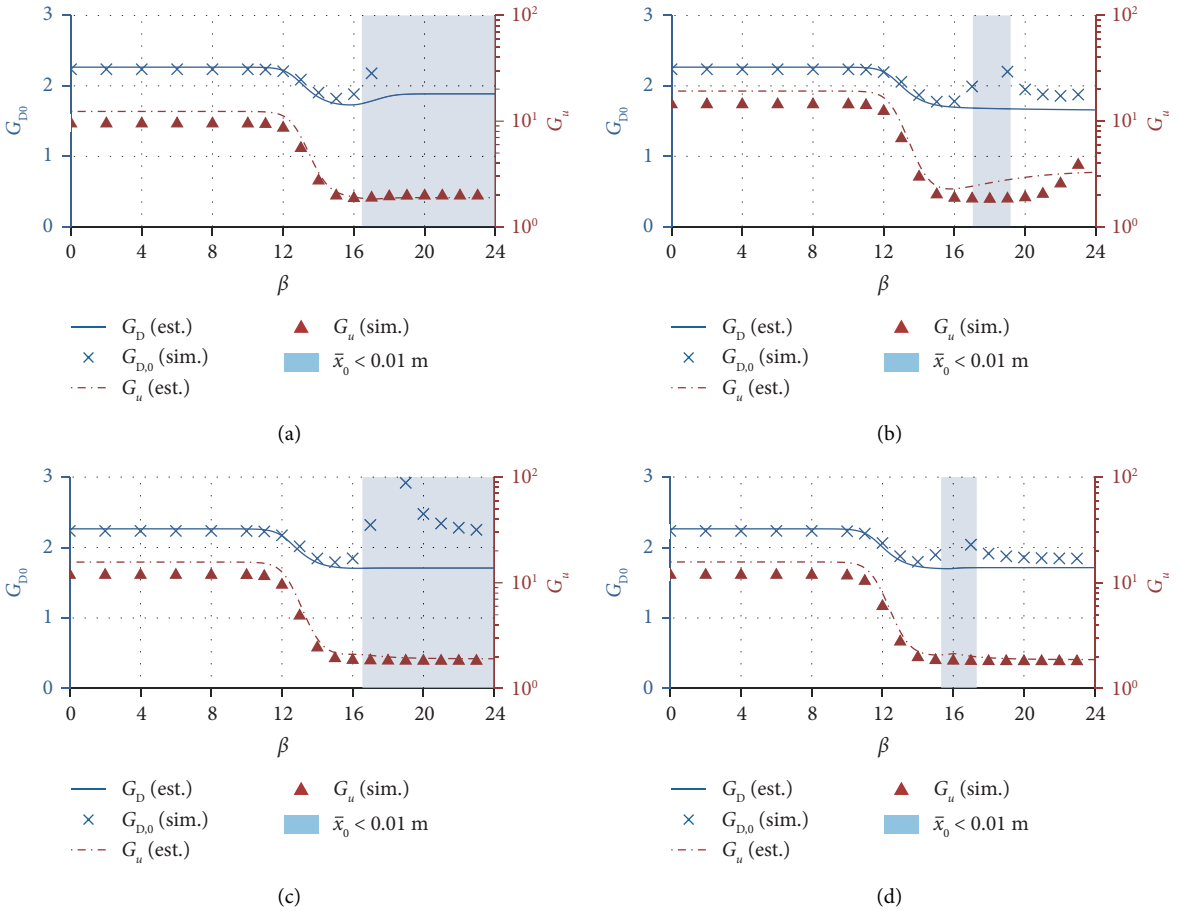

FIGURE 15: Gust factor: estimation vs. simulation result (aspect ratio: 4, return period: 100-year, isolated period: 5 s). (a) Case A. (b) Case B. (c) Case C. (d) Case D.

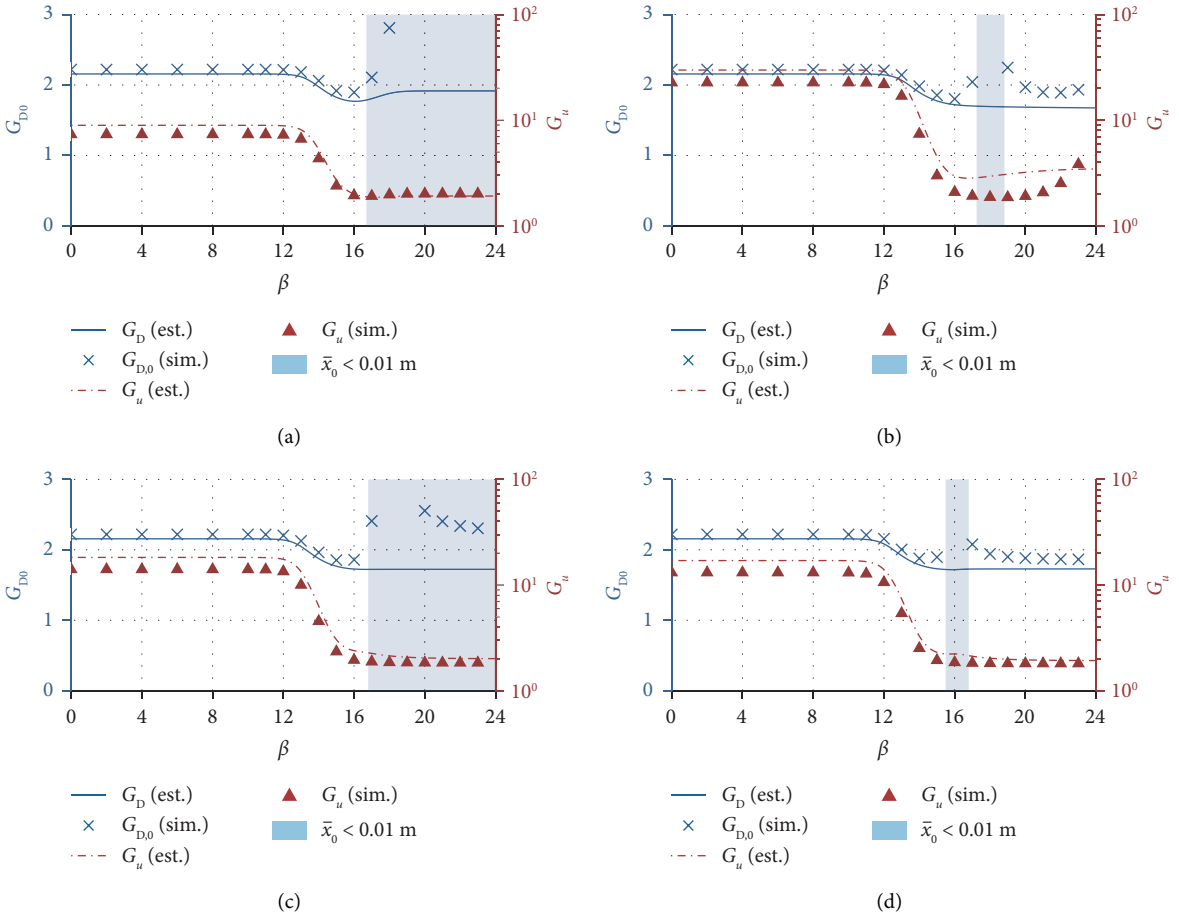

FIGURE 16: Gust factor: estimation vs. simulation result (aspect ratio: 4, return period: 500-year, isolated period: 3 s). (a) Case A. (b) Case B. (c) Case C. (d) Case D.

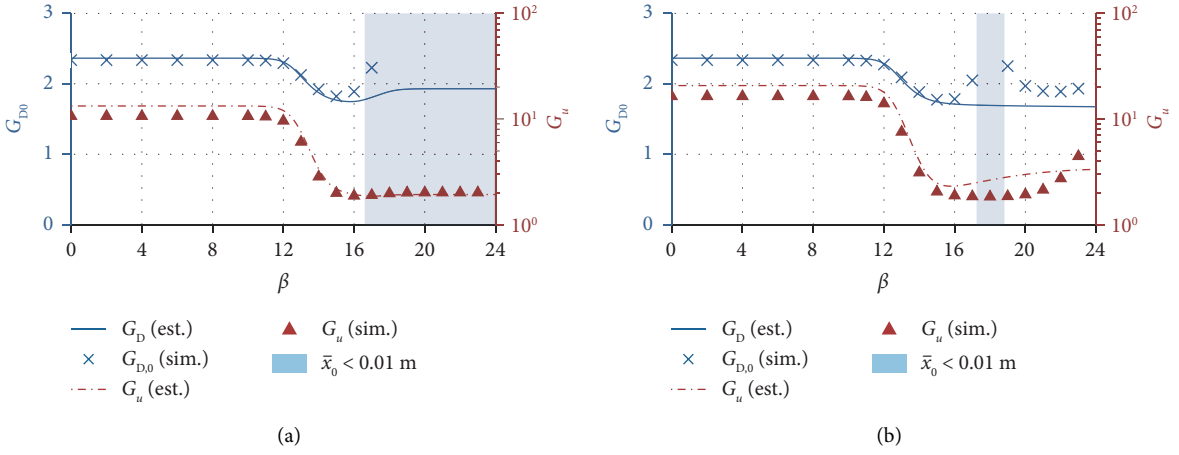

FIGURE 17: Continued.

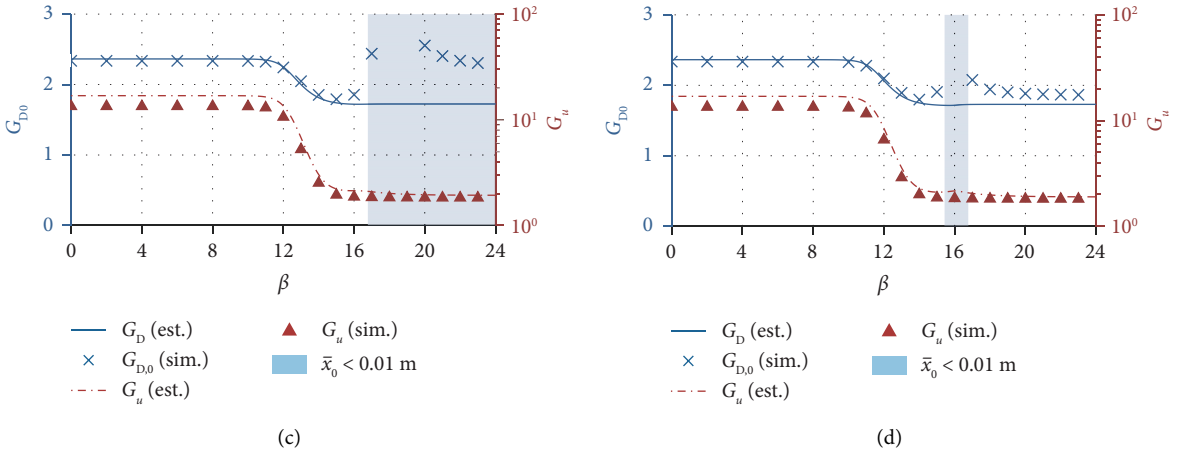

FIGURE 17: Gust factor: estimation vs. simulation result (aspect ratio: 4, return period: 500-year, isolated period: 5 s). (a) Case A. (b) Case B. (c) Case C. (d) Case D.

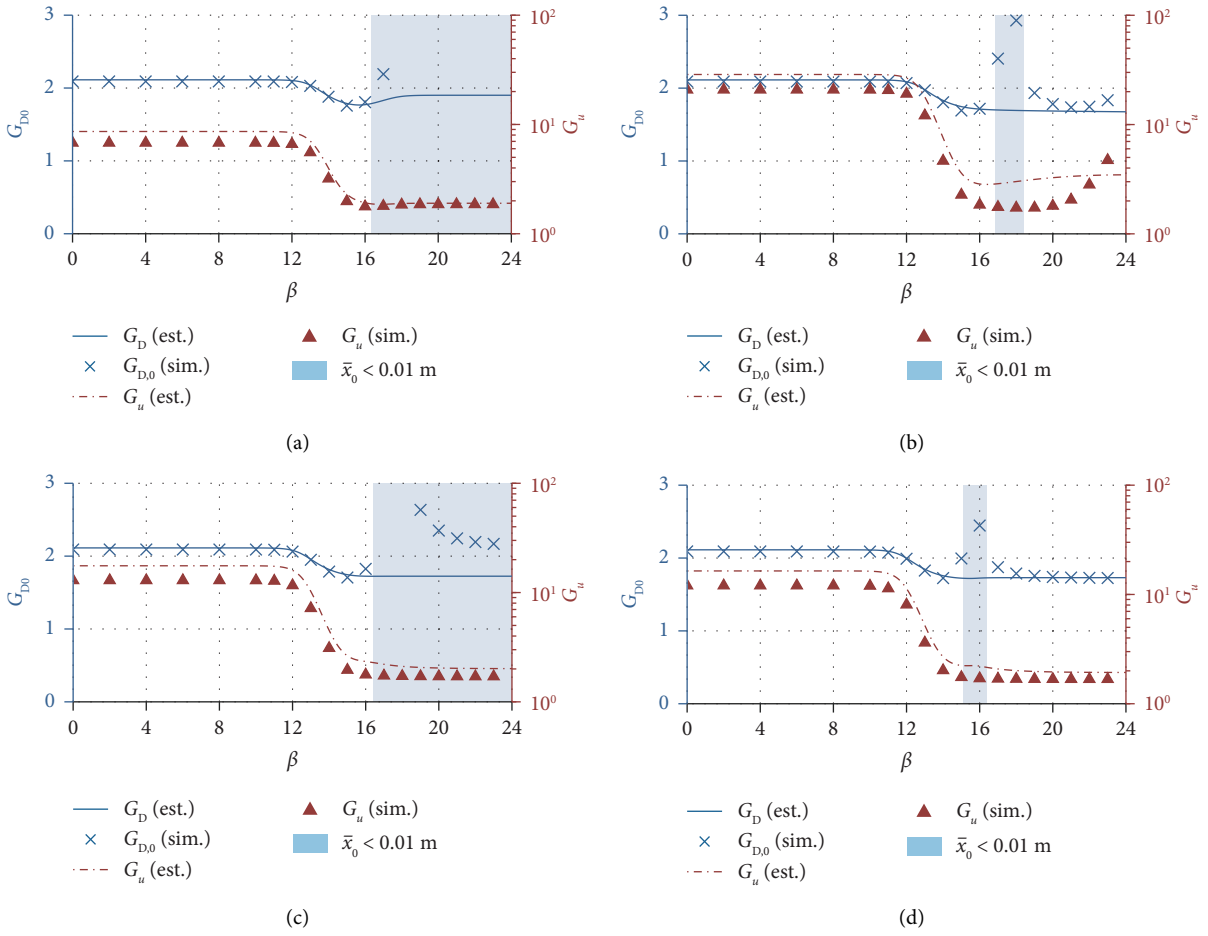

FIGURE 18: Gust factor: estimation vs. simulation result (aspect ratio: 5, return period: 100-year, isolated period: 3 s). (a) Case A. (b) Case B. (c) Case C. (d) Case D.

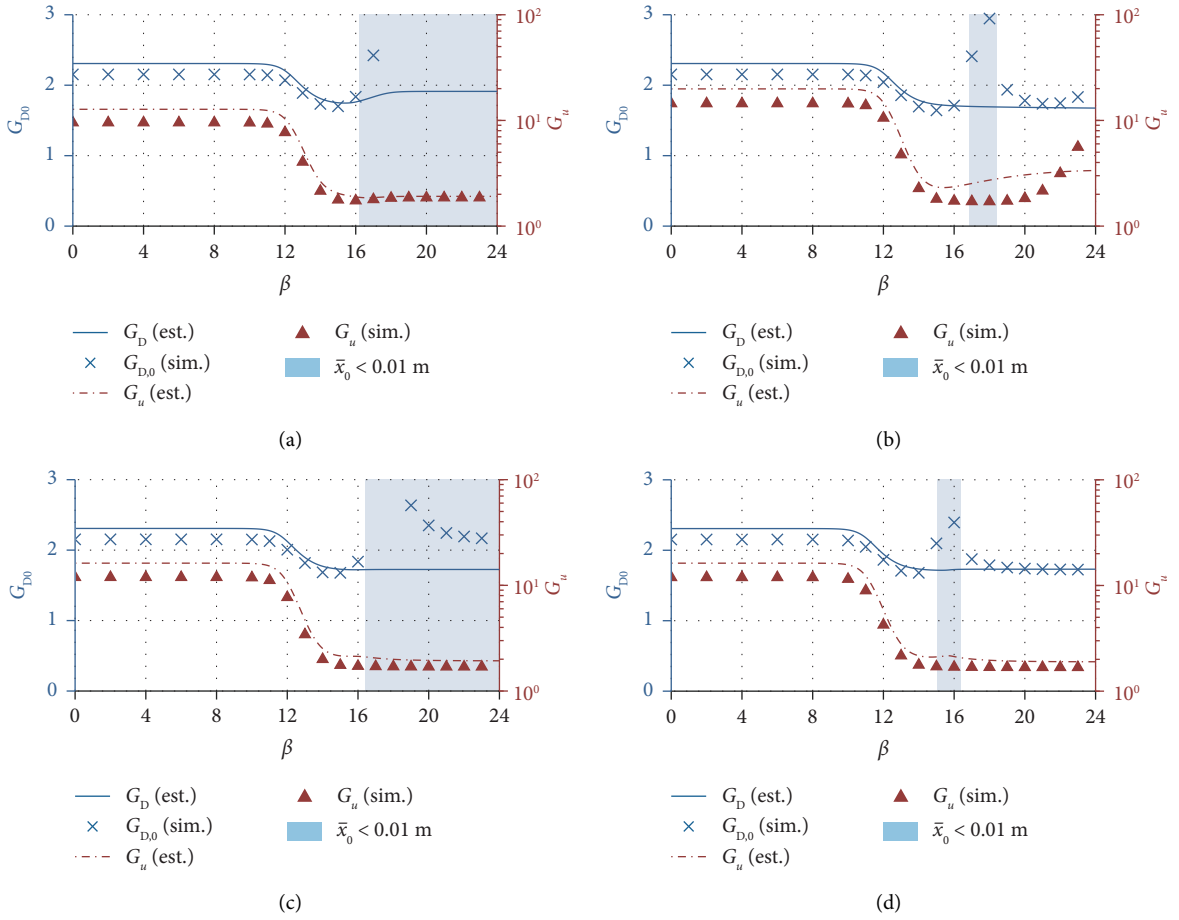

Figure 19: Gust factor: estimation vs. simulation result (aspect ratio: 5, return period: 100-year, isolated period: 5 s). (a) Case A. (b) Case B. (c) Case C. (d) Case D.

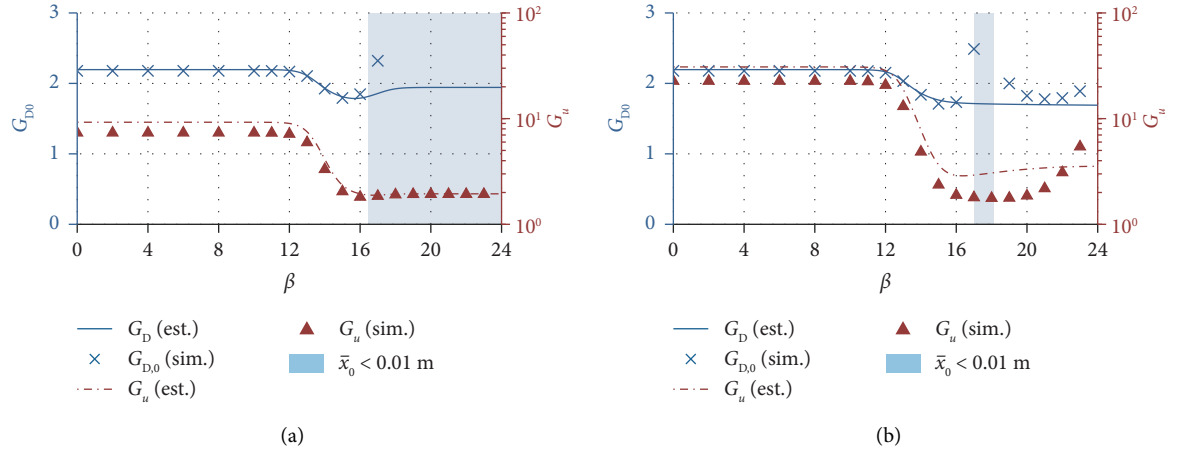

Figure 20: Continued.

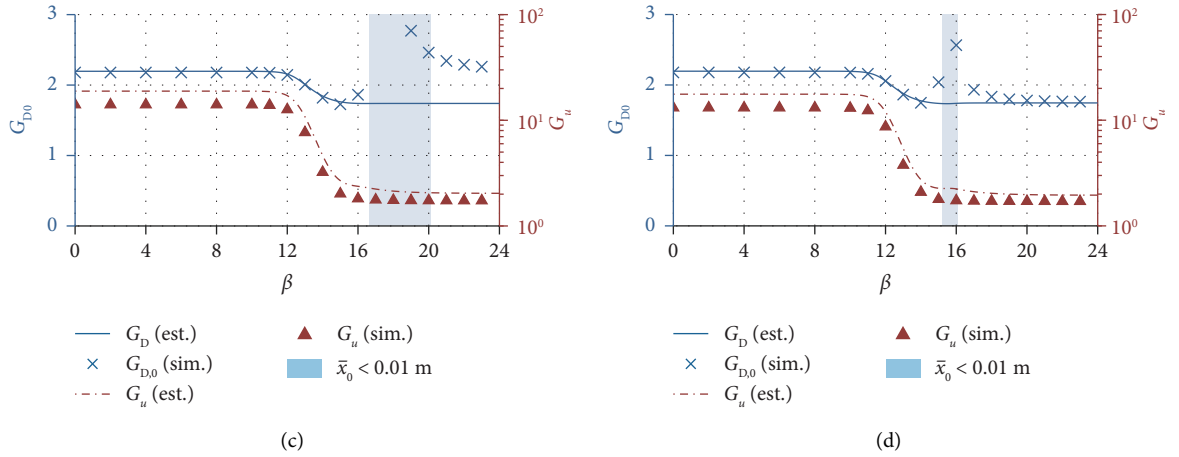

FIGURE 20: Gust factor: estimation vs. simulation result (aspect ratio: 5, return period: 500-year, isolated period: 3 s). (a) Case A. (b) Case B. (c) Case C. (d) Case D.

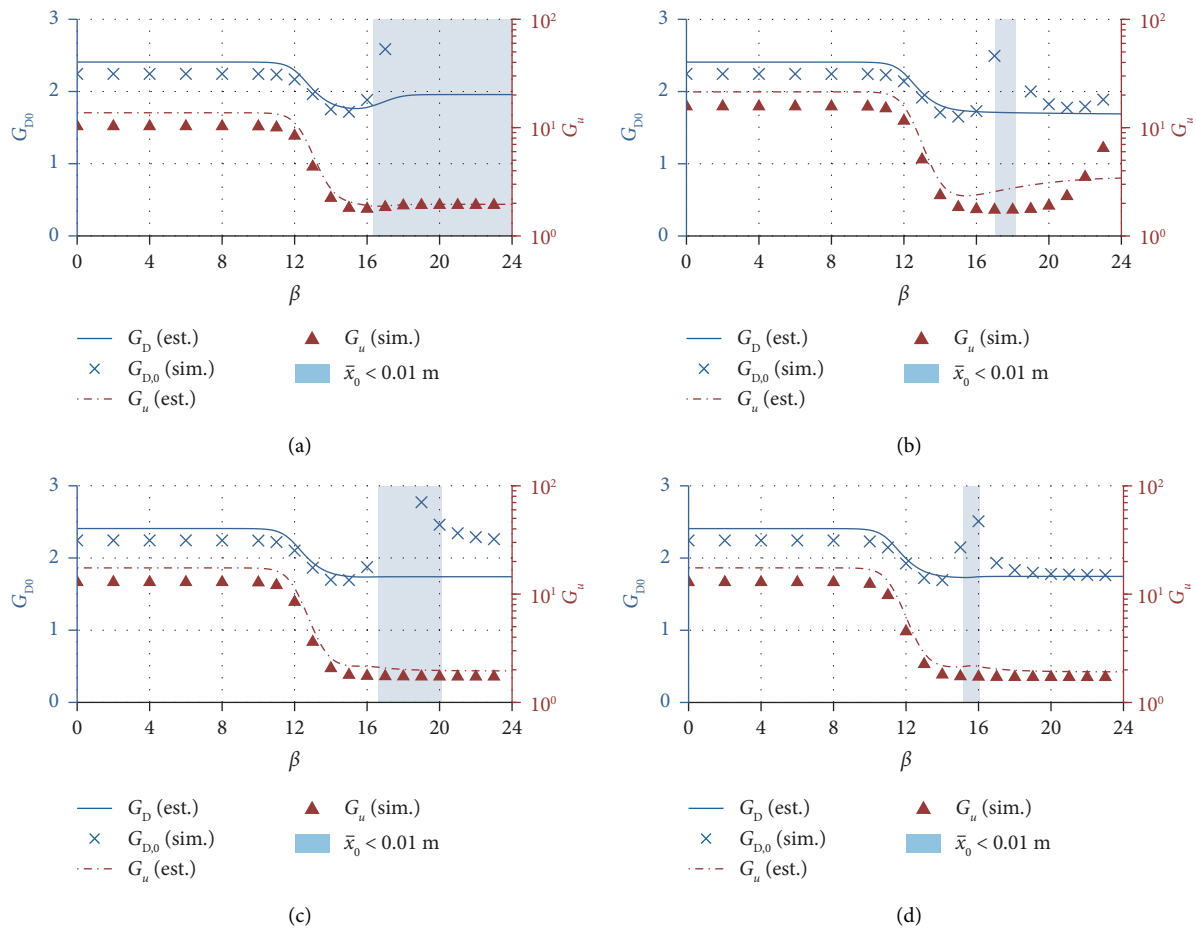

FIGURE 21: Gust factor: estimation vs. simulation result (aspect ratio: 5, return period: 500-year, isolated period: 5 s). (a) Case A. (b) Case B. (c) Case C. (d) Case D.

(iii) The mean control force increases monotonically with the weighting coefficient β.

(iv) The mean displacement of the base-isolation story may be suppressed to the negative direction of wind if weighting entries of the superstructure is not 0 (cases 2 ~ 4).

(v) The mean control force of case 1 is smaller than that of cases 2 ~ 4.

Figure 10 presents the comparison of the gust factors for displacement and control force between the estimations (equations (23) and (35)) and simulation results. From Figure 10, the following results are obtained:

(vi) The estimated values of the gust factors for displacement align well with the simulation results if the mean displacement of the isolation story, $\overline{x}_0$, is larger than 0.01 m.

(vii) The estimation error of the gust factors for displacement is relatively large for the cases that $\overline{x}_0 < 0.01$ m.

(viii) The estimation values of the gust factors for control force match well with the simulation results for all cases.

(ix) The gust factors for displacement and control force decreases as the weighting coefficient β increases.

Therefore, the effectiveness of the proposed estimation methods is validated.

This section only presented the validations of the proposed estimation methods considering different LQR weighting matrices. Appendix C provides numerical verifications that incorporate feedback gain, aspect ratio, wind force return period, and isolation natural period as parameters.

7. Conclusion

This paper proposed a straightforward method for estimating the maximum displacement responses and maximum control force for active base-isolation systems. An equivalent passive model of the active base-isolation system has been conceived to theoretically describe the vibration characteristics of the system. Utilizing the constructed equivalent model, a strategy was devised to compute the mean response and mean control force of the model when subjected to along-wind forces. Subsequently, we devised gust factors for displacement and control force that estimate the maximum response and maximum control force. Compared with the previous method, this method has the following two advantages:

(1) Instead of solving a complex equation, which contains high-dimensional matrices, we devised a new method to compute the mean displacement and mean control force only using the static equilibrium of the equivalent passive model, which is easily to understand for structural designers.

(2) The gust factor for control force proposed in this paper does not restrict the selection of LQR weighting matrices, extending its scope of application.

This approach dispenses with the need for numerical simulations, thereby simplifying conventional design processes for active base-isolation. Numerical examples, which incorporate feedback gain, aspect ratio, wind force return period, and isolated period as parameters, verified the effectiveness of the presented methods.

From the numerical examples, the following results are obtained:

(i) The mean displacement of the isolation story decreases as the weighting coefficient β increases.

(ii) The mean control force increases monotonically with the weighting coefficient β.

(iii) The mean displacement of the base-isolation story may be suppressed to the negative direction of wind if weighting entries of the superstructure is not 0 (cases 2 $\sim$ 4).

(iv) The mean control force of case 1 is smaller than that of cases 2 $\sim$ 4.

(v) The gust factors for displacement and control force decreases as the weighting coefficient β increases.

Appendix

A. Comparison of Cases with Nonzero Weighting Entries for Velocity

This section presents a comparison between the cases where $q_{V,i} \neq 0$ (velocity component) and the cases where $q_{V,i} = 0$ (shown in Table 4).

Table 6 show the four cases of weighting entries **Q** used in this section. Note that compared with cases A $\sim$ D, cases A$'$ $\sim$ D$'$ assign the same weighting entries for both displacement and velocity of the same stories.

Figure 11 shows a comparison of the maximum displacements between cases A $\sim$ D and cases A$'$ $\sim$ D$'$. Note that the weighting coefficients β of each case are set to the same value, 24, to achieve relatively high control performance. From Figure 11, the following results are obtained:

(i) The maximum displacement response of case A$'$ is almost the same as case A.

(ii) The maximum displacement response of cases B$'$ $\sim$ D$'$ is much larger than that of cases B $\sim$ D.

Given these observations, this paper will only consider cases A $\sim$ D, because adding weighting entries to the velocity component may increase the maximum displacement, which is not desirable for wind-resistant design.

B. Comparison of Gust Factor Estimation for Control Force: Previous Method vs. New Method

This section elucidates the comparative assessment of gust factor calculations for control force, contrasting the previous method [20] with the new method proposed in Section 5.

The respective equations employed for estimating the gust factor for control force are delineated in the following:

Previous method:

$$G_u = G_D + G_V, \tag{B.1a}$$

$$G_V = (G_D - 1)\omega_{m1}\frac{\mathbf{K_{PV}}\overline{\mathbf{X}}}{\mathbf{K_{PD}}\overline{\mathbf{X}}}. \tag{B.1b}$$

New method (this paper):

$$G_u = \sqrt{G_D^2 + G_V^2}, \qquad G_V = (G_D - 1)\omega_{m1}\frac{\mathbf{K_{PV}}\boldsymbol{\Phi}_{m1}}{\mathbf{K_{PD}}\boldsymbol{\Phi}_{m1}}. \tag{B.2}$$

From the aforementioned equations, two discernible differences are observed between the previous method and the new approach.

(i) The previous method uses an absolute sum to estimate the maximum control force, whilst the new methodology utilizes the square root of the sum of squares (SRSSs). The reason that we use SRSS is because a phase difference between displacement and velocity is commonplace, which means that maximum displacement and velocity typically do not occur simultaneously.

(ii) The previous methodology uses the mean-displacement vector to compute the mean control force, whereas the new approach utilizes the 1st mode vector. The reason for using the 1st mode vector instead of the mean-displacement vector is that the angle of the mean-displacement vector varies as the mean displacement is suppressed (see Figure 12). This alteration affects the result of the dot product as depicted in (B.1b).

Figure 13 shows a comparison of the previous method and the new method for estimating the gust factor for control force. From Figure 13, it is discernible that the new method provides superior estimation accuracy for all tested cases.

Figure 12 represents the angle, θ_D, between the mean displacement vector and the 1st mode vector of the system. The formal definition of θ_D is provided in the following:

$$\theta_D = \cos^{-1}\frac{\bar{\mathbf{x}} \cdot \varphi_{m1}}{\|\bar{\mathbf{x}}\| \, \| \varphi_{m1} \|}. \tag{B.3}$$

In this context, "·" and "‖ ‖" denote the dot product and norm of a vector, respectively.

According to Figure 12, it can be seen that θ_D increases as the weighting coefficient, β, increases. Therefore, substituting the mean displacement vector with the first mode vector can significantly enhance the estimation accuracy.

C. Parametric Investigation for Gust Factors

This section presents numerical validations of the proposed gust factor estimation equations, specifically, equations (23) and (34), using variable parameters such as the aspect ratio of the building, return period of wind force, and isolated period. Parameters for the models used in this section are listed in Table 7.

Figures 14–21 show numerical validations for the cases listed in Table 7. From Figures 14–21, the following observations are obtained:

(i) When the mean displacement of the isolation story, $\underline{x}_0$, exceeds 0.01 m, the gust factor estimates for displacement closely align with the simulation results.

(ii) For all considered cases, the gust factor estimates for control force exhibit close agreement with the simulation results.

From the abovementioned results, the efficacy of the proposed gust factor estimation equations, (23) and (34), is validated.

Data Availability

The data used to support the findings of this study are available from the corresponding author upon request.

Conflicts of Interest

The authors declare that they have no conflicts of interest.

Acknowledgments

This work was supported in part by the Collaborative Research Projects of Laboratory for Materials and Structures, the Institute of Innovative Research, Tokyo Institute of Technology. Open access funding was enabled and organized by JUSTICE Group 1 2023.

References

[1] S. Nagarajaiah, K. Zou, and S. Herkal, "Reduction of transmissibility and increase in efficacy of vibration isolation using negative stiffness device with enhanced damping," *Structural Control and Health Monitoring*, vol. 29, no. 11, 2022.

[2] K. Miyamoto, J. Iba, K. Watanabe, K. Ishii, and M. Kikuchi, "Development of nonlinear geometric seismic isolation with a duffing spring," *Structural Control and Health Monitoring*, vol. 2023, Article ID 3917013, pp. 1–24, 2023.

[3] F. Mazza, "Effects of the long-term behaviour of isolation devices on the seismic response of base-isolated buildings," *Structural Control and Health Monitoring*, vol. 26, no. 4, p. e2331, 2019.

[4] M. Omiya and H. Kitamura, "Investigation and analysis on the structural characteristics of the recent base isolated buildings corresponding to long-period ground motion [in Japanese]," *AIJ journal of technology and design*, vol. 25, no. 59, pp. 61–66, 2019.

[5] L. Wang, S. Nagarajaiah, W. Shi, and Y. Zhou, "Seismic performance improvement of base-isolated structures using a semi-active tuned mass damper," *Engineering Structures*, vol. 271, 2022.

[6] L. Wang, Y. Zhou, S. Nagarajaiah, and W. Shi, "Bi-directional semi-active tuned mass damper for torsional asymmetric structural seismic response control," *Engineering Structures*, vol. 294, 2023.

[7] Y. Arcan and U. Yalcincan, "Soil-structure interaction consideration for base isolated structures under earthquake excitation," *Buildings*, vol. 13, no. 4.

[8] The Japan Society of Seismic Isolation, "Progression of planning for seismic-isolated buildings [in Japanese]," https://www.jssi.or.jp/wordpress/wp-content/uploads/2022/12/2021-datasyuseki.pdf.

[9] Z.-X. Li, D. Wen, Y. Shi, and X. Wei, "A frequency-dependent variable-damping control based variable-orifice damper for smart base-isolation system," *Smart Materials and Structures*, vol. 31, no. 12, 2022.

[10] H. Sheikh, N. C. Van Engelen, and R. Ruparathna, "A review of base isolation systems with adaptive characteristics," *Structures*, vol. 38, pp. 1542–1555, 2022.

[11] H. Yao, P. Tan, H. Zhou, and F. Zhou, "A composite control scheme for electromagnetic active mass damper against control-structure-interaction effects," *Engineering Structures*, vol. 281, 2023.

[12] The Japan Society of Seismic Isolation, *Activity Report of the Committee on the Study of Next-Generation Seismic Isolation Systems*, The Japan Society of Seismic Isolation, Japan, 2022.

[13] A. Kareem and Y. Zhou, "Gust loading factor—past, present and future," *Journal of Wind Engineering and Industrial Aerodynamics*, vol. 91, no. 12-15, pp. 1301–1328, 2003.

[14] Y. Liu, G. A. Kopp, and S. F. Chen, "An examination of the gust effect factor for rigid high-rise buildings," *Frontiers in Built Environment*, vol. 6, 2021.

[15] V. Kumar Elumalai and R. Ganapathy Subramanian, "A new algebraic LQR weight selection algorithm for tracking control of 2 DoF torsion system," *Archives of Electrical Engineering*, vol. 66, no. 1, pp. 55–75, 2017.

[16] C. Horiguchi and M. Kohiyama, "Simultaneous optimization of structural and control systems of a SDOF buildings with a linear quadratic regulator controller aiming at performance-based design," *Journal of Structural and Construction Engineering (Transactions of AIJ)*, vol. 77, no. 675, pp. 715–722, 2012.

[17] D. Sato, Y. Chen, K. Miyamoto, and J. She, "A spectrum for estimating the maximum control force for passive-base-isolated buildings with lqr control," *Engineering Structures*, vol. 199, 2019.

[18] Y. Chen, D. Sato, K. Miyamoto, and J. She, "Control-force spectrum considering both natural period and damping ratio for active base-isolated building," *Actuators*, vol. 11, no. 6, p. 156, 2022.

[19] Y. Chen, D. Sato, K. Miyamoto, and J. She, "Response-spectrum-based design method for active base-isolated buildings with viscous dampers and hysteretic dampers," *Mechanical Systems and Signal Processing*, vol. 180, 2022.

[20] Y. Chen, D. Sato, K. Miyamoto, and J. She, "Estimating the maximum response and maximum control force for high-rise base-isolated buildings with active structural control in along-wind direction," *Engineering Structures*, vol. 216, 2020.

[21] The Japan Society of Seismic Isolation, *Guidelines for the Wind-Resistant Design of Seismically Base-Isolated Buildings*, The Japan Society of Seismic Isolation, Japan, 2018.

[22] D. Sato, K. Kasai, and T. Tamura, "Influence of frequency sensitivity of viscoelastic damper on wind-induced response [in Japanese]," *Journal of Structural and Construction Engineering (Transactions of AIJ)*, vol. 74, no. 635, pp. 75–82, 2009.

[23] H. Marukawa, T. Ohkuma, H. Kitimura, K. Yoshie, T. Tsurumi, and D. Sato, "Energy input of local wind forces for high-rise building based on wind tunnel test: Part.2 local wind force characteristics of rectangular high-rise buildings," in *Summaries of Technical Papers of Annual Meeting of Architectural Institute of Japan*, p. 193, Architectural Institute of Japan, Tokyo, Japan, 2010.

[24] G. Saito, D. Sato, K. Yoshie, T. Ohkuma, J. Katagiri, and H. Kitamura, "Influence of number of wind-force samples on response of high-rise base-isolated building using elastoplastic model [in Japanese]," *AIJ Journal of Technology and Design*, vol. 23, no. 53, pp. 65–70, 2017.

[25] Architectural Institute of Japan, *AIJ Recommendations for Loads on Buildings*, Architectural Institute of Japan, Japan, 015.

[26] L. Wang, S. Nagarajaiah, Y. Zhou, and W. Shi, "Experimental study on adaptive-passive tuned mass damper with variable stiffness for vertical human-induced vibration control," *Engineering Structures*, vol. 280, 2023.

[27] L. Wang, Y. Zhou, and W. Shi, "Seismic response control of a nonlinear tall building under mainshock–aftershock sequences using semi-active tuned mass damper," *International Journal of Structural Stability and Dynamics*, vol. 23, no. 16, 2023.

[28] H. Zhang, L. Wang, and W. Shi, "Seismic control of adaptive variable stiffness intelligent structures using fuzzy control strategy combined with lstm," *Journal of Building Engineering*, vol. 78, 2023.

[29] R. Dorf and R. Bishop, *Modern Control Systems*, Pearson Education Limited, London, UK, 2017.

[30] Y. Ikeda, "Active and semi-active control of buildings in Japan," *Journal of JAEE*, vol. 4, no. 3, pp. 278–282, 2004.

[31] L. Koutsoloukas, N. Nikitas, and P. Aristidou, "Passive, semi-active, active and hybrid mass dampers: a literature review with associated applications on building-like structures," *Developments in the Built Environment*, vol. 12, 2022.

[32] R. E. Skelton, T. Iwasaki, and K. M. Grigoriadis, *A Unified Algebraic Approach to Control Design*, Taylor & Francis, Oxfordshire, UK, 1997.

[33] A. Preumont and A. Seto, *Active Control of Structures*, John Wiley & Sons Inc, Hoboken, NJ, USA, 2008.

[34] Y. Arcan, "Absolute instantaneous optimal control performance index for active vibration control of structures under seismic excitation," *Shock and Vibration*, vol. 2019, Article ID 4207427, 4 pages, 2019.

[35] Y. Chen, D. Sato, K. Miyamoto, and J. She, "Method of designing control system for high-rise seismically isolated buildings with active control under along-wind force," *Journal of Structural Engineering*, vol. 64, pp. 199–206, 2018.